AIAA JOURNAL
Vol. 52, No. 9, September 2014

Hypersonic Aeroelastic and Aerothermoelastic Studies Using Computational Fluid Dynamics

Nicolas Lamorte* and Peretz P. Friedmann*
University of Michigan, Ann Arbor, Michigan 48109-2140

DOI: 10.2514/1.J053018

A framework for aerothermoelastic-stability-boundary calculation for hypersonic configurations using computational fluid dynamics combined with radial basis functions for mesh deformation is developed. Application of computational fluid dynamics enables one to consider different turbulence conditions, laminar or turbulent, and different models of the air mixture, in particular real-gas model, which accounts for dissociation of molecules at high temperature. The effect of transition on the flutter margin of the heated structure is also considered using an uncertainty-propagation framework. The aerothermoelastic-stability margin of a three-dimensional low-aspect-ratio wing, representative of a control surface of a hypersonic vehicle, is investigated for various flight conditions. The system is found to be sensitive to turbulence modeling, as well as the location of the transition from laminar to turbulent flow. Real-gas effects play a minor role for the flight conditions considered. This study demonstrates the advantages of accounting for uncertainty at an early stage of the analysis, and emphasizes the important relation between transition from laminar to turbulent, thermal stresses, and stability margins of hypersonic vehicles.

Nomenclature

$[\mathbf{A}]$	=	transition matrix in the time domain
A_r	=	reaction-rate parameter
A, B	=	beta-distribution coefficients
a_i	=	average regression coefficient
$\mathbf{C_A}$	=	aerodynamic-influence damping matrix
c	=	chord
c_m	=	specific heat of the material
c_p	=	specific heat at constant pressure
c_v	=	specific heat at constant volume
E_a	=	activation energy
e_a	=	air internal energy
f	=	quantity of interest
f_i	=	natural frequency
H	=	altitude
H_f	=	altitude of the trajectory
h_a	=	air enthalpy
h_w	=	aerodynamic heat-flux coefficient
$\mathbf{I}$	=	identity matrix
$\mathbf{K}$	=	structural stiffness matrix
$\mathbf{K_A}$	=	aerodynamic-influence stiffness matrix
k	=	reaction-rate coefficient
k_x, k_y, k_z	=	thermal conductivity
M	=	Mach number
$\mathbf{M}$	=	structural mass matrix
$\mathbf{M_A}$, $\mathbf{C_A}$, $\mathbf{K_A}$	=	apparent mass matrix
M_{fc}	=	flutter Mach number of the cold structure
M_{fm}	=	flutter margin of the hot structure
N_I	=	number of integration points
N_m	=	number of modes
n	=	temperature exponent in rate-coefficient expression
P	=	pressure
p	=	polynomial function
p_f	=	probability of failure
p_i	=	root of the aeroelastic-stability equation
Q_i	=	generalized aerodynamic load
$\dot{q}_{\text{aero}}$, $\dot{q}_{\text{rad}}$, $\dot{q}_{\text{cond}}$, $\dot{q}_{\text{st}}$	=	heat transfer rate due to aerodynamic heating, radiation, conduction, and stored energy
q_i	=	generalized degree of freedom
q_∞	=	freestream dynamic pressure
R	=	perfect-gas constant
r	=	$\|\boldsymbol{x}\|$; Euclidian distance from the origin
T	=	temperature
T_{AW}	=	adiabatic-wall temperature
T_E	=	kinetic energy
T_R	=	equilibrium-radiation temperature
t	=	time
t_f	=	time to buckling
U_E	=	elastic energy
U_∞	=	freestream velocity
v_n	=	velocity in the z direction
w	=	structural deformation in the z direction
$\boldsymbol{X}$	=	$\{\mathbf{q}; \dot{\mathbf{q}}\}$; state variable
x	=	chordwise coordinate
$\boldsymbol{x}$	=	(x, y, z); vector position
x_{ea}	=	elastic-axis location
x_t	=	transition location from leading edge of the wing in the chordwise direction, positive aft
$\|\boldsymbol{x}\|$	=	$\sqrt{\sum_i x_i^2}$; Euclidian norm
y	=	spanwise coordinate
$Z_s(x, y)$	=	structural shape
z	=	coordinate normal to the wing
$[\alpha]$	=	radial-basis-function coefficients
α_s	=	static angle of attack
γ	=	specific-heat ratio
Δt	=	time step
ϵ	=	emissivity
ζ_i	=	damping coefficient
$\boldsymbol{\Theta}$	=	integral of the state-transition matrix
μ_L	=	laminar viscosity
μ_T	=	turbulent viscosity
ξ	=	uncertain variable
ρ	=	air density
ρ_m	=	material density
σ	=	Stefan–Boltzmann constant
τ	=	thickness ratio
$\boldsymbol{\Phi}$	=	state-transition matrix
ϕ	=	radial basis function

Presented as Paper 2012-1591 at the 54th AIAA/ASME/ASCE/AHS/ASC Structures, Structural Dynamics, and Materials, Boston, MA, 8–11 April 2013; received 21 August 2013; revision received 11 February 2014; accepted for publication 26 February 2014; published online 18 June 2014.

*Department of Aerospace Engineering.

ϕ_i	=	Lagrange polynomial
$\psi_i(x, y, z)$	=	mode-shape deformation in the z direction in the ith mode
$\partial\Omega$	=	wetted surface
ω_{di}	=	$\omega_i\sqrt{1-\zeta_i^2}$; damped frequency
ω_i	=	natural frequency

Subscript

∞	=	freestream conditions

Superscripts

F	=	pertaining to the fluid
S	=	pertaining to the structure
$\hat{}$	=	least-squares estimate
$\cdot$	=	d/dt; differentiation with time

I. Introduction

HYPERSONIC flight is an active area of research motivated by interest in unmanned rapid response to threats and reusable launch vehicles for affordable access to space [1–6]. For hypersonic cruise speeds, airbreathing engines are required for sustained flight [5,7,8]. Atmospheric flight at hypersonic speeds causes severe aerodynamic heating effects. Aerodynamic heating degrades the material properties. Temperature gradients, boundary conditions (BCs), and geometrical constraints introduce thermal stresses that can dramatically affect structural integrity and create local buckling [1]. The accurate modeling of aerothermoelastic interactions is critical for hypersonic-vehicle performance, stability, and reliability analyses.

High-speed flows are inherently complex and involve phenomena not present in supersonic conditions (e.g., dissociations [7–9], chemically reacting flow, viscous interactions, and higher levels of aerodynamic heat flux). Furthermore, there are no suitable high-speed high-enthalpy tunnels that would allow the testing of scaled models of hypersonic vehicles. Also, hypersonic aerothermoelastic scaling laws are not available at high Mach numbers [10]. Therefore, the development of accurate computational aerothermoelastic simulation capabilities is important for the design and analysis of hypersonic vehicles. The hypersonic environment is depicted in terms of altitude and Mach number in Fig. 1. Two isodynamic pressure curves corresponding to $q_\infty = 0.5$ atm and $q_\infty = 1.0$ atm, respectively, are depicted in Fig. 1. The lower dynamic pressure corresponds to a limit under which the scramjet engine cannot function efficiently. The higher limit of 1 atm is the structural limit. Exceeding this limit results in extreme static pressure and thermal loading that practical configurations cannot withstand. The two curves define the hypersonic corridor and illustrate the fact that airbreathing hypersonic vehicles are tightly constrained in their operating environment [11]. Furthermore, the shaded areas correspond to real gas (RG) effects that occur at high speeds corresponding to high static temperatures [7]. The perfect gas (PG) model is sufficient for the airflow for Mach numbers less than 3, but vibration of the biatomic molecules becomes important above this speed. For higher flight Mach numbers, oxygen dissociates first, then nitrogen, and gas ionization occurs at reentry conditions.

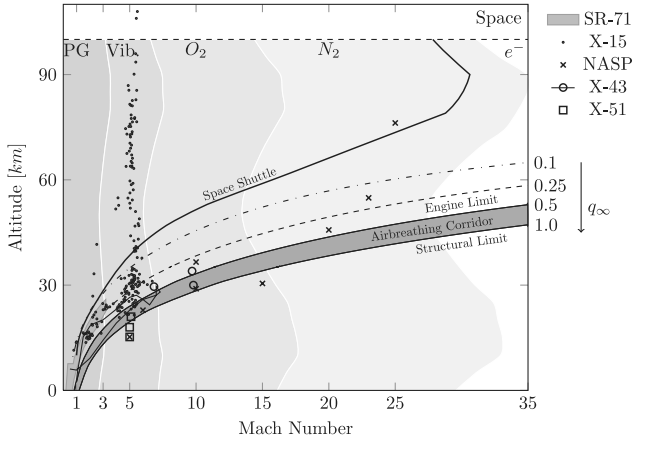

Fig. 1 Flight envelopes of existing and potential hypersonic vehicles.

Flight envelopes of several previous and prospective hypersonic vehicles are shown in Fig. 1. Only a few airbreathing hypersonic vehicles have flown. The X-15 was the first experimental aircraft capable of reaching hypersonic speeds for a limited time, owing to its rocket engine [12]. As preliminary steps toward reaching hypersonic speeds, sustained airbreathing supersonic flights were demonstrated with the F-104 and SR-71 Blackbird [13]. The latter flew at supersonic speeds for extended periods of time in the atmosphere [13]. For the X-15 and SR-71, the structure had to be made of titanium to withstand the thermal loads. The National Aerospace Plane was intended to be an airbreathing hypersonic vehicle capable of long duration flight at hypersonic speeds at the edge of the atmosphere [14,15]. However, the program was canceled due to numerous unresolved technological challenges connected to structural and material reliability at elevated temperatures. More recent scramjet-engine demonstrators are represented by the X-43 and X-51 vehicles. These experimental vehicles were designed to test and advance the scramjet-propulsion technology. Both of them are dropped from the B-52 bomber. A rocket booster accelerates them to high Mach numbers. After separation from the booster, the scramjet engine is turned on. The flights were intended to last for a few hundred seconds. In the case of the X-51, two out of four flights experienced early termination due to the engine's unstart, thermal-management issues, and loss of control.

Piston theory (PT) has been used extensively in numerous studies on hypersonic aeroelasticity, in which deformation is small and the freestream Mach number is higher than 2 [1,16,17]. Third-order PT (3 PT) was successfully used in flutter prediction of a typical supersonic control surface in hypersonic flow, and it was shown to outperform other approximate approaches when compared against computational fluid dynamics (CFD) calculation [1]. In this paper, a new formulation of PT is presented, which shows that 3 PT is only required for capturing the effect of thickness; however, it is not required for capturing the effect of aeroelastic deformation. In this new formulation, the pressure is linearized with respect to the generalized degrees of freedom governing vehicle deformation. This linearized theory produces identical results to conventional 3 PT.

Despite the convenience of PT, CFD is the only alternative that allows increased modeling complexity of the unsteady aerodynamic loading and heating. Coupling of a CFD code with a finite element solver for the heat transfer and structural dynamic equations is considered in this study. The aerothermoelastic-coupling approach combines a thermal solver with an aeroelastic solver. The solution of the Navier–Stokes (NS) equation is obtained using CFD++, a commercial CFD code capable of accounting for dynamic mesh deformation [18]. It provides the aerodynamic pressure and heat-flux distributions at the structural interface, while the heat transfer problem and structural dynamics are represented using the finite element method implemented in MSC.NASTRAN [19].

High-fidelity numerical simulations of the complex hypersonic flow environment are computationally expensive, and the state of the art is still under development [20]. The CFL3D code is an aeroelastic solver developed by the NASA Langley Research Center, which has been used in the hypersonic aeroelastic studies of a hypersonic vehicle and a low-aspect-ratio wing [1]. Yet, the role of various factors such as RG effects, chemically reacting flows, and complex viscous interactions is not well understood. The influence of RG effects and turbulence modeling on the aeroelastic stability of hypersonic-vehicle components (such as a wing representing control surfaces and skin panels) has not been explored in the literature [1]. A previous work that focused on the aeroelastic-stability-boundary calculations [21] is extended in the current study to incorporate aerothermoelastic considerations using the CFD++ code.

In addition to turbulence and gas-model variability, uncertainty in transition location is incorporated to quantify the reliability

associated with the assumption of fully turbulent flows. The most effective approaches for propagating uncertainty are direct Monte Carlo simulations (MCSs) [22] and response-surface-based methods, such as stochastic collocation (SC) or polynomial chaos expansion (PCE). In this study, SC is considered as an effective alternative to direct MCS, which has prohibitive computational costs for complex problems. The SC approach was shown to outperform the PCE in a recent study [23], and was successfully used to propagate uncertainty in aeroelastic and aerothermoelastic analyses of a hypersonic vehicle [24], as well as integrated propulsion–airframe analysis [25].

The overall objective of this study was to develop a framework for hypersonic aerothermoelastic studies using CFD simulations with mesh deformation based on radial basis functions (RBFs) combined with a computational structural dynamic model. The four specific objectives of the paper were:

1) Present a new linearized formulation of PT that is useful for aeroelastic-stability calculations, and compare it to 3 PT and CFD-based predictions.

2) Examine coupling using a mesh-deformation scheme employing RBFs for aeroelastic calculations.

3) Assess the influence of gas and turbulence modeling on hypersonic aeroelastic-stability boundary.

4) Assess the influence of transition location on hypersonic aerothermoelastic stability.

The application of the method is illustrated for a three-dimensional low-aspect-ratio wing, representative of a control surface of a hypersonic vehicle.

II. Overview of the Aerothermoelastic Framework

Computational costs for a tightly coupled analysis representing the entire trajectory of a hypersonic-vehicle structure subject to aerodynamic heating and pressure loading are excessive. Therefore, various approximations are introduced to reduce the computational costs to manageable levels. One of these approximations is a loosely coupled aerothermoelastic analysis, in which the heat flux is not affected by the structural deformation. This approximation is justified by characteristic timescales between structural vibrations and the heat-flux calculations [26]. The complete aerothermoelastic analysis is illustrated by the flowchart in Fig. 2. It combines a loosely coupled thermoelastic analysis with an aeroelastic solver. In both analyses, the solution of the NS equations is obtained using the commercial software CFD++, capable of accounting for dynamic mesh deformation and different gas models. The various components of this framework are described next.

A. Thermal Analysis

The heat transfer problem is treated using CFD to evaluate the aerodynamic heat flux combined with a finite element model (FEM) solver for determining the temperature distribution. The heat transfer problem is governed by Eq. (1) and schematically depicted in Fig. 3. Figure 3 illustrates that the load-carrying structure is combined with a thermal protection system (TPS) composed of two layers: a thermal insulation and a radiation shield. At the surface of the TPS, the aerodynamic heat flux $\dot{q}_{\text{aero}}$ and the radiation heat flux $\dot{q}_{\text{rad}}$ are in equilibrium with the conductive heat flux $\dot{q}_{\text{cond}}$ and the variation of energy stored in the TPS, $\dot{q}_{\text{st}}$, as given by Eq. (2).

$$\rho_m c_m \frac{\partial T}{\partial t} = k_x \frac{\partial^2 T}{\partial x^2} + k_y \frac{\partial^2 T}{\partial y^2} + k_z \frac{\partial^2 T}{\partial z^2} \tag{1}$$

$$\dot{q}_{\text{aero}} = \dot{q}_{\text{rad}} + \dot{q}_{\text{cond}} + \dot{q}_{\text{st}}, \qquad \text{in which } \dot{q}_{\text{aero}} = h_w(T_{\text{AW}} - T) \tag{2}$$

The flux equilibrium in steady state yields an algebraic equation, Eq. (3), for the radiation equilibrium temperature T_R, which corresponds to maximum surface temperatures:

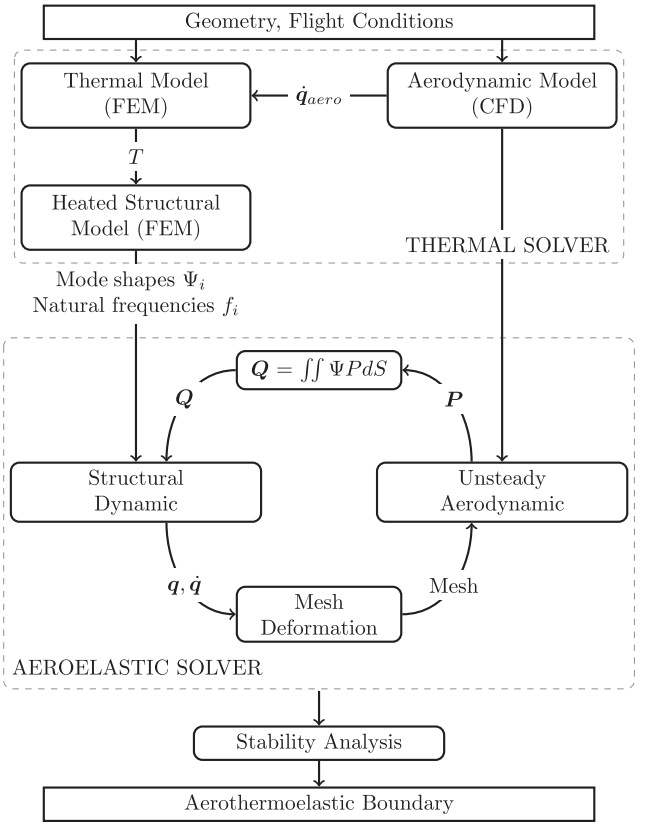

Fig. 2 Aerothermoelastic framework.

$$h_w(T_{\text{AW}} - T_R) = \sigma \epsilon T_R^4 \tag{3}$$

Because thermal degradation, thermal stresses, and heat transfer are coupled with each other, heat-flux prediction is a key component of the analysis. The aerodynamic heat flux $\dot{q}_{\text{aero}}$ is obtained using CFD++. The calculation of the heat-flux coefficient h_w and the adiabatic-wall temperature are obtained by using CFD++ twice for a particular flight condition: once with adiabatic-wall BC to determine T_{AW} and once with constant wall temperature BC to calculate h_w. Both quantities are used to define the BCs of the heat transfer problem in the FEM solver. The heat flux is calculated with a CFD mesh that is finer than the FEM mesh. When applying the aerodynamic heat load at the surface of the FEM mesh, the total heat flux applied to the structure is equal to that provided by the fluid solver.

As illustrated in Fig. 2, the heated modes are obtained in two steps. First, the temperature distributions in the structure and the TPS layer are calculated with the MSC.NASTRAN (Sol. 159) solving the heat transfer problem with appropriate BCs, as given in Eqs. (1) and (2). The temperature distribution of the undeformed structure is calculated as a function of time for the entire trajectory. Next, the heated modes are obtained from the temperature distribution in the wing. The nonlinear solver MSC.NASTRAN (Sol. 106) is used to

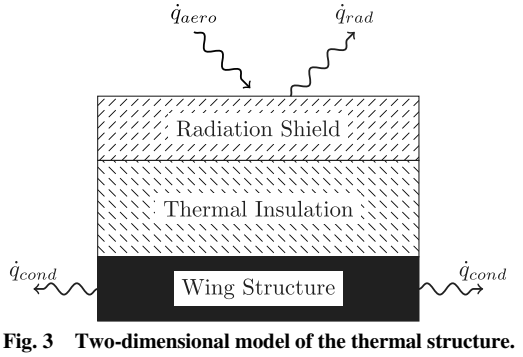

Fig. 3 Two-dimensional model of the thermal structure.

calculate the normal modes of the heated structure. Thermal stresses and material properties that are functions of temperature are included. The thermal coupling is a one-way coupling that implies that the heat flux is not affected by deformation or by the wall temperature. The heated modes and modal frequencies are used in the aeroelastic solver described next.

B. Aeroelastic Analysis

The aeroelastic simulation is indicated in the lower portion of Fig. 2, and enclosed by a dashed line. The structure is represented by a limited number of mode shapes, Ψ, computed using a FEM obtained with MSC.NASTRAN. The equations of motion (EOM) are integrated using a predictor/corrector explicit scheme that requires the evaluation of the generalized loads only once per time step. At each time step, the deformation of the structure is passed to the mesh-deformation routine, which is independent from MSC.NASTRAN and CFD++. The fluid mesh is deformed using RBF, and the updated nodal positions and velocities are passed to the fluid solver. The CFD solution is marched in time for the deformed configuration using a point-implicit scheme. The generalized loads, $\boldsymbol{Q}$, are calculated based on the pressure distribution at the wetted interface. Finally, the structural deformation is advanced to the next time step. Eventually, the transient aeroelastic response is obtained. The stability of the aeroelastic system is determined using a system identification (SI) approach that extracts the damping from the response.

1. *Formulation of the EOM*

The EOM represent the heated structure; thus, the mode shapes and frequencies are functions of the temperature distribution in the structure. This dependency is kept in an implicit form for conciseness. Hypersonic-vehicle structures undergo small deformations, and the structure is represented by a limited number of its natural modes [27]. The in-plane displacements of the wing, u and v, are assumed to be negligible. The out-of-plane displacement, $w(t, \boldsymbol{x})$, at any point of the structure is described by a finite series of modes given by Eq. (4):

$$w(t, \boldsymbol{x}) = \sum_{i=1}^{N_m} q_i(t)\psi_i(\boldsymbol{x}) \tag{4}$$

The EOM of the aeroelastic system obtained from Lagrange equations is given in Eq. (5):

$$\frac{\mathrm{d}}{\mathrm{d}t}\left(\frac{\partial T_E}{\partial \dot{q}_i}\right) - \frac{\partial T_E}{\partial q_i} + \frac{\partial U_E}{\partial q_i} = Q_i \qquad i = 1, \ldots, N_m \tag{5}$$

From Eq. (5), the final EOM can be written as in Eq. (6):

$$\mathbf{M}\ddot{\boldsymbol{q}} + \mathbf{K}\boldsymbol{q} = \boldsymbol{Q}(t, \boldsymbol{q}, \dot{\boldsymbol{q}}, \ddot{\boldsymbol{q}}) \tag{6}$$

The coupling algorithm between the CFD solver and the structural solver employed in solving the EOM is described next.

2. *Time Integration and Fluid–Structure Coupling*

The fluid and the structure are coupled through the generalized loads. The EOM in the state-vector form can be written as Eq. (7):

$$\{\dot{\boldsymbol{X}}\} = [\mathbf{A}]\{\boldsymbol{X}\} + [\mathbf{B}]\{\boldsymbol{Q}\} \tag{7}$$

in which

$$\{\boldsymbol{X}\} = \begin{Bmatrix} \boldsymbol{q} \\ \dot{\boldsymbol{q}} \end{Bmatrix} \qquad [\mathbf{A}] = \begin{bmatrix} \mathbf{0} & \mathbf{I} \\ -\mathbf{M}^{-1}\mathbf{K} & \mathbf{0} \end{bmatrix} \qquad [\mathbf{B}] = \begin{Bmatrix} \mathbf{0} \\ \mathbf{M}^{-1} \end{Bmatrix} \tag{8}$$

In this framework, the matrix $[\mathbf{A}]$ is constant for each aeroelastic calculation. The EOM can be integrated exactly in time, and the solution is given by Eq. (9). The first term corresponds to the homogeneous response of the structure, and the second term accounts for the effect of the aerodynamic loads.

$$\boldsymbol{X}_{n+1} = e^{[\mathbf{A}]\Delta t}\boldsymbol{X}_n + \int_{t_n}^{t_{n+1}} e^{[\mathbf{A}](t_{n+1}-\tau)}[\mathbf{B}]\boldsymbol{Q}(\tau, \boldsymbol{X})\,\mathrm{d}\tau \tag{9}$$

The transient response of the aeroelastic system is integrated in time using an explicit method combining a second-order Adams–Bashforth predictor [28] and a trapezoidal corrector, as given in Eqs. (10) and (11), respectively.

$$\tilde{\boldsymbol{X}}_{n+1} = \boldsymbol{\Phi}\boldsymbol{X}_n + \frac{\boldsymbol{\Theta}}{2}[3\boldsymbol{Q}(\boldsymbol{X}_n, t_n) - \boldsymbol{Q}(\boldsymbol{X}_{n-1}, t_{n-1})] \tag{10}$$

$$\boldsymbol{X}_{n+1} = \boldsymbol{\Phi}\boldsymbol{X}_n + \frac{\boldsymbol{\Theta}}{2}[\boldsymbol{Q}(\tilde{\boldsymbol{X}}_{n+1}, t_{n+1}) + \boldsymbol{Q}(\boldsymbol{X}_n, t_n)] \tag{11}$$

In Eqs. (10) and (11), the state-transition matrix $\boldsymbol{\Phi}$ and the integral of the state-transition matrix $\boldsymbol{\Theta}$ are given in Eqs. (12) and (13), respectively.

$$\boldsymbol{\Phi} = e^{[\mathbf{A}]\Delta t} \tag{12}$$

$$\boldsymbol{\Theta} = \int_{t_n}^{t_{n+1}} e^{[\mathbf{A}](t_{n+1}-\tau)}[\mathbf{B}]\,\mathrm{d}\tau = [\mathbf{A}]^{-1}(\Phi - \mathbf{I})[\mathbf{B}] \tag{13}$$

The state-transition matrix $\boldsymbol{\Phi}$ is calculated using the Padé approximation with scaling and squaring [29] implemented in MATLAB's expm function. The time marching is illustrated in Fig. 4. At the beginning of each time step, the structural deformation at time t_{n+1} is estimated using the generalized loads at the previous and current time steps as given by the predictor step, Eq. (10), and represented by the dashed arrows in Fig. 4. Next, the fluid mesh is deformed based on the predicted structure deformation, shown by the arrow indicated by $\tilde{\boldsymbol{q}}_{n+1}$. The pressure distribution is updated by multiple subiterations within a time step of the CFD solver to march the NS solution to the next time step, as represented by the dotted arrow. The small circles represent symbolically the subiterations of the CFD solver within the time step. Finally, the generalized loads are transferred to the structural solver, and the deformation of the structure at time $t_n + \Delta t$ is updated using the corrector step given by Eq. (11) based on the generalized loads calculated at time t_{n+1}. The corrector step is represented by the arrow $\tilde{\boldsymbol{Q}}_{n+1}$.

The coupling between the fluid and the structure depends on both the mesh-deformation method and the calculation of the generalized loads.

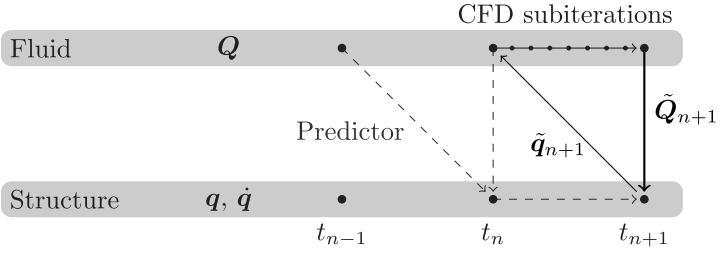

Fig. 4 Time marching and coupling approach.

3. Computation of the Generalized Aerodynamic Loads

The generalized loads are defined by Eq. (14):

$$Q_i(t, \boldsymbol{q}, \dot{\boldsymbol{q}}, \ddot{\boldsymbol{q}}) = \int_{\partial\Omega} -\psi_i(\boldsymbol{x}) P(\boldsymbol{x}, \boldsymbol{q}, \dot{\boldsymbol{q}}, \ddot{\boldsymbol{q}}) n_z \, \mathrm{d}S \qquad 1 \le i \le N_m \tag{14}$$

The calculation of the generalized aerodynamic loads is performed using the CFD mesh. The integration over the surface of the wing, $\partial\Omega$, is replaced by the summation of the contribution of the faces of the fluid cells, $\partial\Omega_k$, that define the wing. The modal shape function, ψ_i, is evaluated at the centroid of each face, $\boldsymbol{x}_k$, to express the generalized loads, as given by Eq. (15):

$$Q_i \simeq \sum_{k=1}^{N_{\text{cells}}} \psi_i(\boldsymbol{x}_k) \int_{\partial\Omega_k} -P(\boldsymbol{x}) n_z \, \mathrm{d}S \tag{15}$$

The quantity $\int_{\partial\Omega_k} -P(\boldsymbol{x}) n_z \, \mathrm{d}S$ is the contribution of one face to the force in the z direction. It is extracted from the CFD++ code by means of an output file after each time step. The CFD++ code cannot calculate the Q_i values; therefore, verification of this calculation is infeasible. However, for a sanity check, the resultant forces and moments can be calculated in a similar manner, and compared to the ones calculated by the CFD++. To calculate the resultant forces in the vertical direction, $\psi_i(\boldsymbol{x}_k) = 1$ is used, and $\psi_i(\boldsymbol{x}_k) = x_k - x_{\text{ea}}$ for the moment in the y direction. The results show perfect agreement with the present approach. This integration is consistent with the pressure discretization associated with the CFD algorithm in the CFD++. Consequently, the only approximation made in this approach comes from the calculation of the shape function at the centroid. For consistency, this value is given by the RBF method chosen to deform the mesh, presented next.

4. Mesh Deformation Using RBF

A radial function (RF), ϕ, is a scalar function whose value depends only on the distance from the origin, $r = \|\boldsymbol{x}\|$. RBF networks are an effective tool for multivariate interpolation of both scattered and gridded data [30]. In aeroelastic applications, the displacement w and velocities $\dot{w}$ are the quantities being interpolated from the fluid–structure interface to the rest of the CFD mesh. Given a set of N_s sampling points, also called driving points, $\boldsymbol{x}_j$, at which the deformation is known: $(\boldsymbol{x}_j, w_j)_{j=1,N_s}$, the RBF interpolant of w, $\hat{w}$ is constructed in the form given by Eq. (16). The interpolated value at a new point, $\boldsymbol{x}$, depends only on the Euclidian distance between $\boldsymbol{x}$ and the driving points $(\boldsymbol{x}_{dj})_{j=1,N_s}$.

$$\hat{w}(\boldsymbol{x}) = \sum_{j=1}^{N_s} \alpha_j \phi(\|\boldsymbol{x} - \boldsymbol{x}_j\|) + p(\boldsymbol{x}) \tag{16}$$

In Eq. (16), the polynomial $p(\boldsymbol{x})$ and the fitting coefficients α_j are determined, such that the interpolant, $\hat{w}$, is equal to the structural deformation w at the sampling points. In the RBF approach, several components have to be chosen to obtain the best fit possible, such as the polynomial order, the choice of RF, and the set of driver points. For aeroelastic simulations, a polynomial of order 1 is considered, such that rigid-body motions are captured by the polynomial component. The RF, volume spline, is chosen: $\phi(\|\boldsymbol{x} - \boldsymbol{x}_{dj}\|) = \|\boldsymbol{x} - \boldsymbol{x}_{dj}\|$.

The choice of the driving points is important. The deformation of the fluid–structure interface is known at the FEM nodes. Several alternative approaches can be used to deform the fluid mesh based on this information. One approach interpolates the deformation from the FEM nodes to the fluid mesh. In this case, the driving points are the FEM nodes on the interface between the structure and the fluid. Because of the global form of the RBF interpolant, the deformed interface defined by the fluid mesh does not coincide exactly with the structural one for fluid points located between adjacent FEM nodes. The FEM mesh is usually coarse when compared to the fluid mesh, as illustrated schematically in Fig. 5. A simplified CFD mesh is deformed using the FEM nodes at the interface as driving points. The FEM deformed interface is represented by the thick dotted line in Fig. 5, and the CFD interface by the thin line with crosses in Fig. 5; the interfaces do not match.

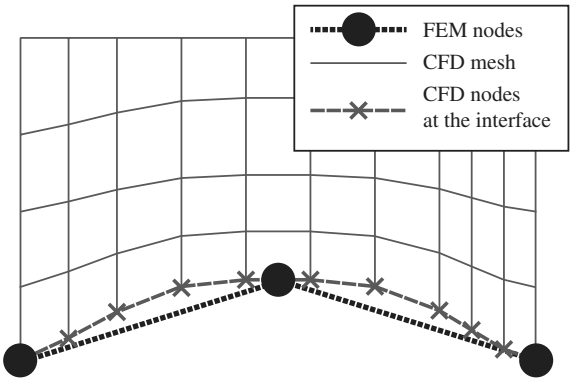

Fig. 5 Illustration of the usage of RBF for mesh deformation.

To ensure that the structure and fluid boundaries match, the set of FEM nodes is augmented with additional driving points at which the deformation is calculated based on the FEM. If necessary, every fluid node of the interface can be used as driving points, and an RBF interpolation based on these points is generated for interior points. This second approach is used in this study. The deformation of the interface at the fluid mesh is calculated using a piecewise bilinear interpolation between the FEM nodes.

C. PG and RG Modeling

The CFD++ code is a modern and effective commercially available code for the solution of the compressible unsteady Reynolds-averaged NS equations [18]. The solutions of the NS equations obtained from the CFD++ capture the complex airflow over the structure, and account for viscous and high-temperature effects. The CFD++ code solves the NS equations using a point-implicit finite volume approach, and a one-equation Spalart–Allmaras (SA) turbulence model is used in this study. Two convenient models of the fluid are available: PG and thermally imperfect or ideal gas (IG), as given in Table 1. Chemical reactions can also be incorporated to account for the dissociation of molecules at high temperatures; for this case, the model is referred to as RG.

For both PG and IG models, the fluid is modeled by a single species, and there is no chemical reaction. Pressure, temperature, and density are related by the same equation of state. In the PG model, the specific heats are constant. Therefore, internal energy e_a and enthalpy h_a are linear functions of temperature. The specific-heat ratio, $\gamma = c_p/c_v$, is constant and assumed to be equal to 1.4. Under these assumptions, limitations of the model manifest themselves at high speed. Thus, this model is often deemed to be inadequate for hypersonic high-altitude flight or reentry problems, in which high gas temperatures are accompanied by nonequilibrium flows [7].

For IG, specific heats are not constant with temperature, as illustrated in the expression of internal energy and enthalpy in Table 1. Similarly, γ is a function of temperature. Polynomial fitting using experimental data can estimate the internal energy and enthalpy of air as functions of temperature. In IG, the compression ratio can increase up to 20, and produce a significant reduction in the stagnation temperature when compared to PG prediction.

Details of a simple RG model, taken from [31], are given in Table 2. It contains five species and eight reactions to account for the

Table 1 PG and IG models

	PG	IG
Equation of state	$P = \rho RT$	
Internal energy	$\partial e_a = c_v \partial T$	$\partial e_a = c_v(T) \partial T$
Enthalpy	$\partial h_a = c_P \partial T$	$\partial h_a = c_P(T) \partial T$
γ	$\gamma =$ constant	$\gamma(T)$

Table 2 Reactions

Reactions	η	A_r, cm^3/mol	$(E_a/R)(K)$	
$O_2 + M \rightarrow 2O + M$	−1.50	2.0×10^{21}	59,500	$M = N_2, O_2, NO$
$O_2 + M \rightarrow 2O + M$	−1.50	1.0×10^{22}	59,500	$M = N, O$
$N_2 + M \rightarrow 2N + M$	−1.60	7.0×10^{21}	113,200	$M = N_2, O_2, NO$
$N_2 + M \rightarrow 2N + M$	−1.60	3.0×10^{22}	113,200	$M = N, O$
$NO + M \rightarrow N + O + M$	0.00	5.0×10^{15}	75,500	$M = N_2, O_2, NO$
$NO + M \rightarrow N + O + M$	0.00	1.1×10^{17}	75,500	$M = N, O$
$N_2 + O \rightarrow NO + N$	−1.00	6.4×10^{17}	38,400	— —
$NO + O \rightarrow O_2 + N$	0.00	8.4×10^{12}	19,450	— —

dissociation of O_2, N_2, and NO. Chemical equilibrium is assumed, and there is no ionization. For each reaction, the reaction constant is given by $k = A_r T^{\eta} \exp[-(E_a/RT)]$.

A computationally efficient model of the aerodynamic loads is presented next.

D. New Formulation of PT and Its Use for Load Calculation

In PT, the pressure at a given location on a moving surface is a point function of the deformation and velocity of the surface, given by Eq. (17):

$$\frac{P(\boldsymbol{x},t)}{P_\infty} = \left[1 + \frac{\gamma-1}{2}\frac{v_n}{a_\infty}\right]^{2\gamma/\gamma-1} \tag{17}$$

The normal velocity of the structure, v_n, given by Eq. (18), is a function of the cross-sectional shape, or thickness distribution, Z_s; the angle of attack α_s; and the structural deformation w. The quantity $\partial Z_s/\partial x$ is the thickness ratio $\pm\tau$.

$$\frac{v_n}{a_\infty}(\boldsymbol{x}, w, \dot{w}) = \frac{1}{a_\infty}\frac{\partial w}{\partial t} + M_\infty\left[\frac{\partial}{\partial x}(Z_s + w) + \alpha_s\right] \tag{18}$$

In a modal representation of the structure, the deformation is given by Eq. (4), and v_n can be written as Eq. (19). For brevity, M_n is defined as $M_n = v_n/a_\infty$.

$$\begin{aligned} M_n &= \frac{v_n}{a_\infty}(\boldsymbol{x}; q, \dot{q}) \\ &= \sum_{i=1}^{N_m}\left[\frac{1}{a_\infty}\psi_i\dot{q}_i + M_\infty\frac{\partial\psi_i}{\partial x}q_i\right] + M_\infty\left(\frac{\partial Z_s}{\partial x} + \alpha_s\right) \end{aligned} \tag{19}$$

1. Classical PT

Classical expansions of PT assume small M_n, and the nonlinear relation between pressure and v_n is simplified using a Taylor series expansion. The different orders of the expansion yield polynomial relations between P and v_n with different degrees of accuracy. The classical first-order (1 PT) to 3 PT are given by Eq. (20), in which the order refers to the highest order of M_n that is retained in the expansion:

$$\frac{P(\boldsymbol{x},t) - P_\infty}{P_\infty} \approx \gamma\left[M_n + \frac{\gamma+1}{4}M_n^2 + \frac{\gamma+1}{12}M_n^3\right] \tag{20}$$

In this approach, small static angle of attack, small airfoil thickness, and small deformation are assumed [16,17].

2. Linearized PT

In aeroelasticity, a relation between unsteady pressure (or the loads) and the generalized degrees of freedom is useful. Expanding PT only with respect to the generalized degrees of freedom is an alternative formulation to classical PT. Note that M_n is an affine function of the generalized degrees of freedom, as given in Eq. (19). It combines a linear function of the degrees of freedom and a constant term that accounts for α_s and the thickness of the wing. Combining Eqs. (17) and (19), pressure is given by

$$\begin{aligned} \frac{P(\boldsymbol{x},t)}{P_\infty} = \Bigg[&\underbrace{1 + \frac{\gamma-1}{2}M_\infty\left(\frac{\partial Z_s}{\partial x} + \alpha_s\right)}_{\text{static term}} \\ &+ \underbrace{\frac{\gamma-1}{2}\sum_{i=1}^{N_m}\left(\frac{1}{a_\infty}\psi_i\dot{q}_i + M_\infty\frac{\partial\psi_i}{\partial x}q_i\right)}_{\text{deformation-related term}}\Bigg]^{2\gamma/\gamma-1} \end{aligned} \tag{21}$$

Equation (21) is rewritten as

$$\frac{P(\boldsymbol{x},t)}{P_\infty} = \eta\left[1 + \frac{\gamma-1}{2}\tilde{M}_n\right]^{2\gamma/\gamma-1} \tag{22}$$

in which

$$\eta = \left[1 + \frac{\gamma-1}{2}M_\infty\left(\frac{\mathrm{d}Z_s}{\mathrm{d}x} + \alpha_s\right)\right]^{2\gamma/\gamma-1} \tag{23}$$

$$\tilde{M}_n = \frac{a_\infty}{\tilde{a}}\sum_{i=1}^{N_m}\psi_i\frac{\dot{q}_i}{a_\infty} + M_\infty\frac{\mathrm{d}\psi_i}{\mathrm{d}x}q_i \tag{24}$$

$$\tilde{a} = a_\infty\left[1 + \frac{\gamma-1}{2}M_\infty\left(\frac{\mathrm{d}Z_s}{\mathrm{d}x} + \alpha_s\right)\right] \tag{25}$$

The expression of pressure in Eq. (22) is similar to PT, Eq. (17). The differences are 1) a correction term η and 2) a modified M_n, defined by Eqs. (23) and (24), respectively. The factor η accounts for the nonlinearities present in the undeformed steady state, and corresponds to the ratio between the freestream pressure and the local steady pressure acting on the undeformed geometry. The $\tilde{M}_n$ term has a form similar to M_n used in conventional PT, but only accounts for the structural deformation. It corresponds to a form of local PT with corrected steady pressure ηP_∞ and speed of sound $\tilde{a}$. Equation (22) distinguishes between the static effects (angle of attack and shape) and deformations, q and $\dot{q}$.

Pressure, given by Eq. (22), is expanded in Taylor series with respect to small deformations $\boldsymbol{q}$ and $\dot{\boldsymbol{q}}$, which correspond to small $\tilde{M}_n$ to yield Eq. (26):

$$\frac{P}{P_\infty} = \eta\left[\underbrace{1 + \gamma\tilde{M}_n}_{\text{linear part}} + \gamma\frac{\gamma+1}{4}\tilde{M}_n^2 + \gamma\frac{\gamma+1}{12}\tilde{M}_n^3\right] \tag{26}$$

This expression of pressure is very similar to the classical 1 PT to 3 PT, and is referred to as linearized PT (Lin. PT) in this paper. The only assumption is small deformations as determined by the relations given by Eq. (27). There are no assumptions on α_s and $|\partial Z_s/\partial x|$ to expand Eq. (17).

$$\omega_i\bar{w} \ll a_\infty \quad \text{and} \quad \frac{\bar{w}}{c} \ll \frac{\tilde{a}/a_\infty}{M_\infty} \tag{27}$$

It is relevant to note that the various expansions of PT allow the analytical integration of the pressure loads when using a Rayleigh–Ritz approach. When the integration of the loads is performed

numerically using Gaussian quadrature, there is no analytical or computational benefit in expanding Eq. (17). However, the expansion provides a means for quantifying the degree of nonlinearity in the relation between pressure and deformation.

3. Aerodynamic-Influence Matrices

The aerodynamic-influence coefficients are a convenient approach that allows writing the relation between structural deformation and aerodynamic forces in a linear manner. Retaining only the linear part of the Lin. PT in Eq. (26) allows one to obtain the aerodynamic-influence matrices by identifying the contribution of $\boldsymbol{q}$ and $\dot{\boldsymbol{q}}$ in the expression of the generalized loads given by Eq. (28):

$$\boldsymbol{Q} = -\int_{\partial\Omega} \psi_i P(\boldsymbol{q}, \dot{\boldsymbol{q}}) n_z \, \mathrm{d}S = \mathbf{K_A}\boldsymbol{q} + \mathbf{C_A}\dot{\boldsymbol{q}} \tag{28}$$

The aerodynamic stiffness and damping matrices, $\mathbf{K_A}$ and $\mathbf{C_A}$, are given by Eqs. (29) and (30), respectively:

$$\mathbf{K_A}_{ij} = -\int_{\partial\Omega} \psi_i \gamma M_\infty P_\infty \left[1 + \frac{\gamma-1}{2} M_\infty \left(\frac{\mathrm{d}Z_s}{\mathrm{d}x} + \alpha_s\right)\right]^{\frac{2\gamma}{\gamma-1}-1} \frac{\mathrm{d}\psi_j}{\mathrm{d}x} n_z \, \mathrm{d}S \tag{29}$$

$$\mathbf{C_A}_{ij} = -\int_{\partial\Omega} \psi_i P_\infty \frac{\gamma}{a_\infty} \left[1 + \frac{\gamma-1}{2} M_\infty \left(\frac{\mathrm{d}Z_s}{\mathrm{d}x} + \alpha_s\right)\right]^{\frac{2\gamma}{\gamma-1}-1} \psi_j n_z \, \mathrm{d}S \tag{30}$$

E. Stability-Boundary Calculation

The stability boundary is obtained by identifying the damping in the system using an SI method described in this section, which assumes that the aeroelastic system can be treated as a linear dynamic system. This assumption allows the identification of the frequencies and damping coefficients of the aeroelastic system that are required for determining its stability boundary. In the numerical implementation, the initial conditions are set, such that all components of the modal velocities, $\dot{q}$, are nonzero. This precaution ensures that all the modes are excited. The p-method is a well-known approach for determining the stability of a linear aeroelastic system [32,33]. It requires that the generalized loads to be a known function of the generalized degrees of freedom and their time derivatives, as given in Eq. (31):

$$\mathbf{Q}(t, \boldsymbol{q}, \dot{\boldsymbol{q}}, \ddot{\boldsymbol{q}}) = \mathbf{M_A}\ddot{q} + \mathbf{C_A}\dot{q} + \mathbf{K_A}q \tag{31}$$

Combining Eqs. (6) and (31), and assuming a solution in the form of $\boldsymbol{q} = \boldsymbol{q}_0 e^{pt}$ yield the flutter equation, Eq. (32):

$$\{(\mathbf{M} - \mathbf{M_A})p^2 - \mathbf{C_A}p + \mathbf{K} - \mathbf{K_A}\}\boldsymbol{q}_0 = 0 \tag{32}$$

Solutions of the flutter equation are obtained for the values of p that satisfy the characteristic equation of the aeroelastic system, Eq. (33):

$$\det[(\mathbf{M} - \mathbf{M_A})p^2 - \mathbf{C_A}p + \mathbf{K} - \mathbf{K_A}] = 0 \tag{33}$$

The frequencies and damping of the aeroelastic system are given by the roots, p_i, of Eq. (33). The frequencies and corresponding damping coefficients are uniquely identified by the real and imaginary parts of p_i, Eq. (34):

$$p_i = \zeta_i \omega_i + \boldsymbol{i}\omega_{di} \tag{34}$$

When the aerodynamic loads are computed using unsteady CFD, the analytical form given by Eq. (31) is not available. However, at each time step, the generalized degrees of freedom and generalized loads are calculated and stored. Therefore, the relation between $\boldsymbol{Q}$ and $\boldsymbol{q}, \dot{\boldsymbol{q}}, \ddot{\boldsymbol{q}}$ can be approximated in the form given by Eq. (31).

At this point, note that PT is a quasi-static formulation of the relation between the deformation and unsteady pressure loading, as presented briefly in Sec. II.D: in PT, pressure does not depend on $\ddot{\boldsymbol{q}}$. In addition, it agrees well with CFD in previous studies. Finally, note that the flow is at high speed compared to the structural deformation. Therefore, it is assumed that $\mathbf{M_A}$ is negligible, and $\boldsymbol{Q}$ is given by Eq. (35):

$$\boldsymbol{Q}(t, \boldsymbol{q}, \dot{\boldsymbol{q}}, \ddot{\boldsymbol{q}}) \simeq \mathbf{C_A}\dot{q} + \mathbf{K_A}q \tag{35}$$

A linear least-squares fit is used to estimate the aerodynamic-influence matrices. The estimates of the aerodynamic stiffness and damping matrices are given by solving the least-squares problem stated in Eq. (36):

$$\min_{\hat{K}_{Aij}, \hat{C}_{Aij}} \left(\sum_{k=1,N_t} \|\boldsymbol{Q}_\mathbf{k} - \mathbf{C_A}\dot{\boldsymbol{q}}_\mathbf{k} - \mathbf{K_A}\boldsymbol{q}_\mathbf{k}\|^2 \right) \tag{36}$$

The solution is obtained using a linear least-squares approach [34] given in Eq. (37):

$$[\hat{\mathbf{K}}_\mathbf{A}, \hat{\mathbf{C}}_\mathbf{A}]^T = (\mathbf{X}^T\mathbf{X})^{-1}\mathbf{X}^T\mathbf{Q},$$

$$\text{in which } \mathbf{X} = \begin{bmatrix} \boldsymbol{q}_1 & \cdots & \boldsymbol{q}_{N_t} \\ \dot{\boldsymbol{q}}_1 & \cdots & \dot{\boldsymbol{q}}_{N_t} \end{bmatrix}^T \quad \text{and} \quad \boldsymbol{Q} = \begin{bmatrix} \boldsymbol{Q}_1^T \\ \vdots \\ \boldsymbol{Q}_{N_t}^T \end{bmatrix} \tag{37}$$

This method uses the generalized loads and takes full advantage of all the information available in the computational framework. Note that, for a perfectly linear system, the frequencies and damping coefficients are recovered.

F. Structural Model

The three-dimensional low-aspect-ratio wing is shown in Fig. 6. The wing is similar to the Lockheed F-104 Starfighter wing, and it is representative of the fins or control surfaces of a prospective long-duration, airbreathing hypersonic vehicle. The structural model is extracted based on a nonlinear FEM created in MSC.NASTRAN and previously studied in [27,35].

For aeroelastic-stability prediction, the structure of the wing is represented by five natural modes depicted in Fig. 7. The natural modes are normalized with respect to their modal mass. The 1327 FEM nodes are uniformly distributed on the surface of the wing, as illustrated in Fig. 7. The wing structure is assumed to be made from 2024-T3 aluminum alloy.

For the aerothermoelastic study, the structure is reinforced at the leading edges to prevent early local buckling. Reinforcements were added in the wing. Leading and trailing edges were stiffened [35], resulting in higher natural frequencies given in Table 3. A TPS prevents overheating of the aluminum structure of the wing from aerodynamic heating. The TPS layers are described in [35]. The radiation shield is composed of a 0.45 mm René 41 metal. The thermal insulation layer is made of 3.8 mm flexible Min-K layer. The René 41 heat shield can withstand temperatures up to 1500 K, and is assumed to have an emissivity of 0.85.

III. Uncertainty-Propagation Analysis

Probabilistic approaches can be used to quantify uncertainty effects. In this study, the effects of uncertain inputs ξ are propagated through a computational analysis symbolically represented by f to quantify uncertainty effects on the output of interest $f(\boldsymbol{\xi})$. The uncertainty-propagation analysis is illustrated in Fig. 8. The function f represents the aerothermoelastic-stability analysis.

The probabilistic approach to uncertainty quantification (UQ) consists of the following steps [23–25]:

1) Each uncertain input is treated as a random variable characterized by a probability distribution, $p(\xi)$.

2) Stochastic collocation is used to approximate the computationally expensive functional dependance of the output of interest on the uncertain inputs, that is, $f(\boldsymbol{\xi})$ is approximated.

3) Conventional MCS methods are applied to the computationally efficient approximate representation obtained from SC. The effects of the uncertain inputs on the output of interest are quantified in terms of probability distributions denoted by $p(y)$.

A. Characterization of Input Probability Distribution

The variability associated with an uncertain input is modeled by a probability density function (PDF), $p(\xi)$. Commonly used PDFs include normal, log-normal, exponential, or Cauchy distributions, which are defined on unbounded domains. Using such PDFs may require evaluating the output of interest at input combinations with no physical significance and/or leading to unfeasible computations. In contrast, beta distributions, given in Eq. (38), represent a family of bounded probability distributions, in which the range of the random input variables can be controlled by prescribing bounds. Moreover, the choice of the two parameters A and B permits one to control the PDF shape, as illustrated in Fig. 9. The parameters A and B control the shape of the tail of the PDF at the bounds $\xi = -1$ and $\xi = 1$, respectively. The values $A = 1$ and $B = 1$ yield a nonzero PDF at the two edges. A value for A, B greater than 1 produces a flat tail, as illustrated in Fig. 9. Thus, high values of A and B produce a PDF that assigns small probabilities to uncertain parameters at the outer edges, thus emphasizing the central portion. Thus, uniform, symmetric, or nonsymmetric PDFs can be accommodated over the input range by using beta distributions [36]. A beta distribution corresponding to particular values of A and B is denoted by Beta(A, B).

$$p_{(A,B)}(\xi) = \frac{\Gamma(A+B)}{\Gamma(A)\Gamma(B)} \frac{(1+\xi)^{A-1}(1-\xi)^{B-1}}{2^{A+B-1}} \tag{38}$$

B. Stochastic Collocation

Once the sources of uncertainty are identified and quantified by appropriate probability distributions, the effects of uncertainty can be studied using two types of approaches: intrusive [37–40] and nonintrusive [23,41,42]. Hypersonic aerothermoelastic problems require the use of nonintrusive methods that do not require modifications to the complex comprehensive analysis codes.

Direct MCS is the simplest nonintrusive approach used in relatively simple aeroelastic studies [42–50]. This method requires numerous evaluations of the function of interest (e.g., flutter Mach number) at values of the uncertain inputs dictated by their probability distributions. The computational cost associated with numerous analysis evaluations is prohibitive for complex problems, such as hypersonic aeroelastic and aerothermoelastic analysis. Therefore, SC is employed in this study as a computationally efficient alternative to direct MCS.

In SC, computationally efficient polynomial response surfaces are used to approximate the functional relationship between uncertain inputs ξ and the output of interest $f(\xi)$, in which ξ is a normalized random variable varying between the limits -1 and 1.

$$f(\xi) \approx \hat{f}(\xi) = \sum_{j=1}^{P+1} A_j \phi_j(\xi) \tag{39}$$

The response surface $\hat{f}$ given by Eq. (39) consists of an expansion in terms of polynomial basis functions, $[\phi_j(\xi)]_{1<j<P+1}$, in which A_j are fitting coefficients, and $P+1$ represents the number of basis functions. Once constructed, MCS can be applied to the computationally inexpensive polynomial response surface to obtain the probability distribution associated with the output of interest.

In the current study, the expensive analyses are evaluated at a set of inputs ξ, called collocation points, which correspond to the numerical integration points [23–25].

For beta distributions, the corresponding numerical integration scheme is computed using Gaussian quadrature [51]. For a single random variable, the numerical integration points are the roots of the Legendre polynomial function of degree N_I associated with the beta probability distribution of the input. The numerical integration scheme is exact for polynomial functions of order less than $2N_I - 1$. This method tends to concentrate collocation points in the regions of higher probability.

For the one-dimensional case, the polynomial response surface, given by Eq. (39), is generated using Lagrange polynomials,

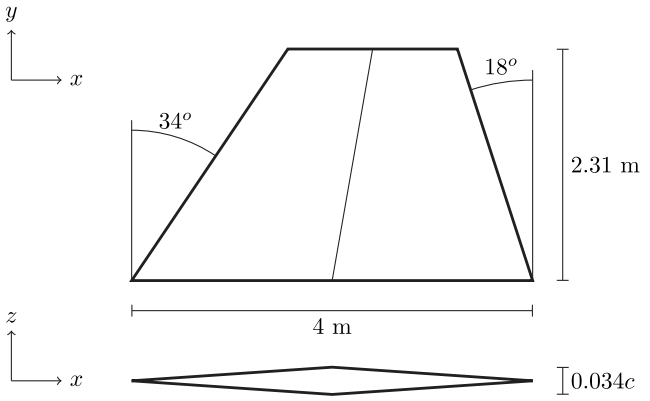

Fig. 6 Three-dimensional low-aspect-ratio wing.

Table 3 Mass and natural frequencies of the wing [35]

	Original wing	Modified wing	Difference, %
Wing mass, kg	350.05	377.73	8
f_1, Hz	13.41	14.28	7
f_2, Hz	37.51	40.94	9
f_3, Hz	49.18	60.06	22
f_4, Hz	77.14	81.86	6
f_5, Hz	79.48	97.25	22

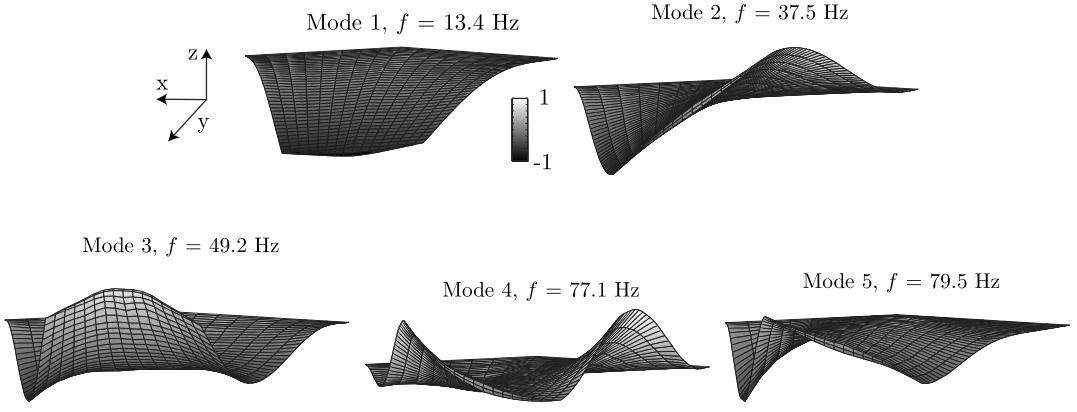

Fig. 7 Structural model for the aeroelastic study based on five modes.

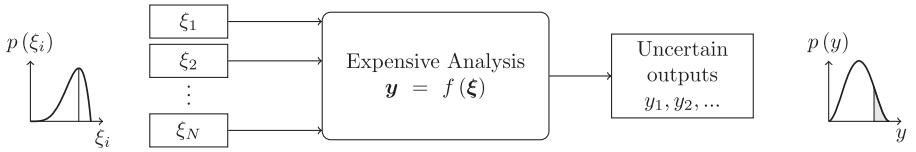

Fig. 8 Uncertainty-propagation approach.

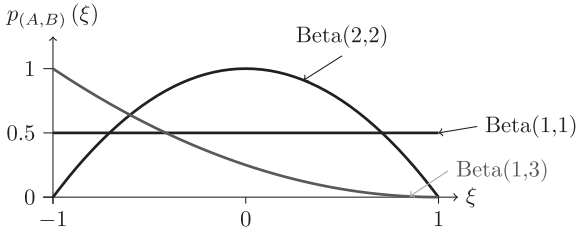

Fig. 9 Examples of beta PDF for different combinations of A and B.

$(\phi_j)_{j=1,P+1}$, Eq. (40), associated with the collocation points, $(\xi_k)_{k=1,N_I}$, Eq. (41):

$$\phi_j(\xi) = \prod_{k=1,k\neq j}^{N_I} \frac{\xi - \xi_k}{\xi_j - \xi_k} \qquad j = 1, P+1 \tag{40}$$

$$\phi_j(\xi_k) = \delta_{jk} \qquad k = 1, N_I \qquad j = 1, P+1 \tag{41}$$

The degree of the polynomial approximation P, in Eqs. (40) and (41), is equal to $N_I - 1$.

Furthermore, the collocation points associated with most integration schemes are located strictly within the domain of the input variable. Therefore, extrapolation is required for response-surface evaluations close to the domain boundaries, which may adversely affect the accuracy.

In the current study, the relation between the uncertain variable and output of interest is highly nonlinear. Therefore, a polynomial response surface does not fit the expensive analysis accurately, and the RBF network, presented in Sec. II.B.4, provides an efficient alternative. The comparison between the performances of the two approaches is described in the Results section.

IV. Results

First, the aeroelastic results are presented. The aerodynamic loading obtained from CFD++ with various gas models and turbulence conditions is compared to 3 PT and CFL3D results for verification purposes. Next, the aerothermoelastic stability of the wing is examined under various turbulence conditions.

A. Aeroelastic Results with PT

The flutter boundary of the low-aspect-ratio wing is computed for different altitudes. Flutter boundaries are given in terms of flutter Mach number and dynamic pressure, and compared to the results of [2] for 3 PT, as presented in Figs. 10a and 10b, respectively. Different forms of PT are used: classical first order (1 PT in Fig. 10), second order (2 PT in Fig. 10), third order (3 PT in Fig. 10) piston theory as well as linearized PT (Lin. PT in Fig. 10). Full order PT (Full PT in Fig. 10) corresponds to the formula without any linearization given in Eq. (18).

Note that 3 PT agrees with the results obtained in [2], which verifies the aeroelastic calculations. Similarly, 1 PT and 2 PT do not give good predictions of the flutter boundary, as shown in previous studies, because they do not account for thickness effects. The stability boundaries obtained with the Lin. PT and Full PT agree with each other perfectly. These results indicate that it is not necessary to use high-order terms for the deformation of the wing in PT as long as the steady state (thickness and angle of attack) is captured accurately. The requirements of using 3 PT are only due to the thickness ($\tau = 3\%$) of the wing, especially at a high Mach number for which $M_\infty \tau$ is large.

Therefore, one can conclude that, for aeroelastic-stability studies, the generalized forces are linear functions of the structural degrees of freedom and their time derivative when using PT. However, the steady part that accounts for the thickness effect and static angle of attack is not small and needs to be captured appropriately by either considering 3 PT or the alternative linearization presented here.

B. Aeroelastic Results with CFD

The computational cost and the parameters associated with the time stepping of the aeroelastic simulations are presented in Table 4. The time step is set to $\Delta t = 1.25 \times 10^{-4}$ s, which corresponds approximately to 100 and 500 time steps per period for the highest and lowest natural frequencies, respectively. A grid-convergence study and time-step convergence study was performed. With one million cells and $\Delta t = 1.25 \times 10^{-4}$ s, the aerodynamic resultants are predicted with less than 1% error when compared to a grid with two million cells or a smaller time step of $\Delta t = 0.625 \times 10^{-4}$ s. Therefore, the CFD calculations are considered converged. Depending on the complexity of the gas model (turbulence, chemistry), the computational time varies from 80 h for laminar flow to 190 h when

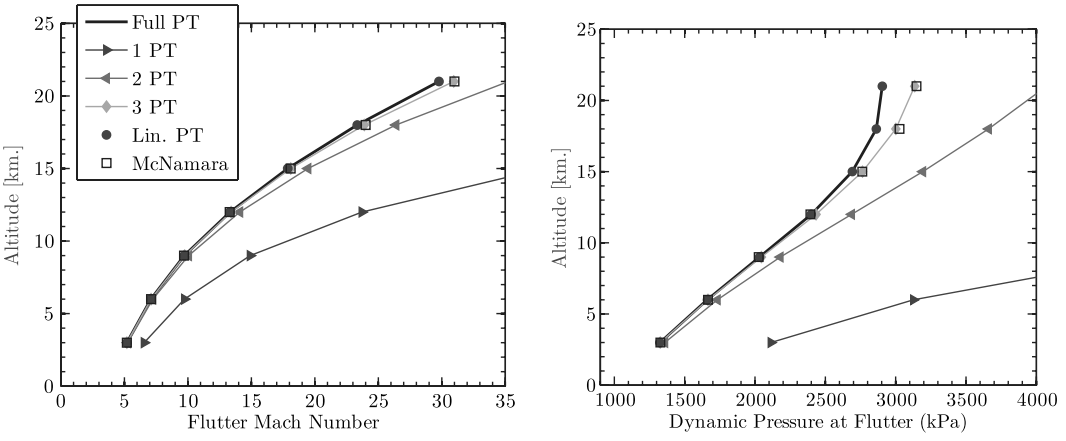

a) Mach number **b) Dynamic pressure**

Fig. 10 Flutter boundary using different orders of PT for the low-aspect-ratio wing.

Table 4 Simulation parameters for three-dimensional calculations

Parameter	
Number of time steps	1000
Time step	0.125 ms
Number of subiterations per time step	50
Number of cells	One million
Number of processors	6
Processor	Opteron 240–254
Computational time	80–190 h

Table 5 Flutter Mach number for the low-aspect-ratio wing using different turbulence and gas models[a]

Gas model	Fluid model	Turbulence model $(\mu_T/\mu_L)\infty$		Flutter Mach number
PG	EU	— —	— —	13.72
	NS	Laminar	— —	13.22
		SA	0.009	12.76
		SA	3	12.78
IG	NS	SA	3	13.0
RG	NS	SA	3	12.87
CFL3D [27]	EU	— —	— —	13.7
	NS	SA modified	0.009	13.65
3 PT		— —	— —	13.4

[a]$H = 12$ km.

chemistry is included. The aeroelastic simulations are performed at constant altitude of 12 km and different Mach numbers. The main contributor to the computational cost associated with the aeroelastic simulations is the CFD calculation. Each aeroelastic simulation requires 2500 initial iterations to converge the steady-state solution of the NS equations of the flow around the wing before the transient aeroelastic response is performed. For each time step, several subiterations of the CFD solver are required to march the fluid in time, as explained previously. At each time step, the new node locations are written in the mesh file, and the CFD code is restarted. It generates a significant amount of additional processing time, which could be eliminated in a fully integrated aeroelastic solver.

The flutter results are presented in Table 5 for an altitude of 12 km. For Euler (EU) aerodynamics, there is a good agreement with CFL3D and the present results. The predicted flutter Mach number is 13.7. In the case of NS aerodynamics, the difference in flutter Mach number between CFL3D and the current simulation can be up to 7%. Adding turbulence reduces the flutter margin. RG effects have a limited impact on the flutter boundary at the flight conditions considered. The examination of the different turbulence models provides additional information explaining the difference between the calculations performed with CFL3D and the current framework. In both CFL3D and CFD++, the SA turbulence model [52] is available and is used for the flutter calculations. In CFL3D, the additional turbulence equation does not require any user input, and the intensity of the freestream turbulence is set by the ratio $(\mu_T/\mu_L)\infty = 0.009$ as boundary and initial condition of the turbulence equation. However, in CFD++, this parameter is a user input, recommended to be taken between 3 and 5 [18].

The results of the flutter analysis are shown in Figs. 11 and 12. The effect of turbulence on flutter-boundary prediction is investigated for various flight conditions in Table 5. EU and laminar flow are compared to turbulent flow for low and high values of freestream turbulence. It illustrates the variability associated with turbulence modeling. Adding turbulence decreases the flutter boundary by up to 7%. An abrupt change is observed when comparing the results for laminar flow, which is close to EU, to the results from turbulent flow. The flutter Mach number predicted in the case of the SA model with $(\mu_T/\mu_L)\infty = 0.009$ is close to the one with $(\mu_T/\mu_L)\infty = 3$. The decrease of flutter boundary with increasing turbulence may be due to the thicker boundary layer for the more turbulent cases, which in turn can produce a higher static pressure on the airfoil due to the thicker effective shape, and explain the decrease in flutter onset. The effect of gas modeling is negligible for the flight condition considered.

In Fig. 11, flutter analyses are given for various turbulence modeling assumptions. Figure 11a depicts the frequencies of the aeroelastic system as a function of flutter Mach number. The different types of lines correspond to different turbulence assumptions. In Fig. 11b, only the damping coefficients corresponding for the first two modes are shown. The frequencies of the aeroelastic system are not sensitive to the model considered. The flutter Mach number predicted using NS for both CFL3D and CFD++ is smaller than the one obtained with EU. Adding turbulence increases the effective shape due to the presence of the boundary layer, and eventually results in an increased local pressure on the wing and a decrease in flutter Mach number.

The results of the flutter analysis are shown in Fig. 12 for different gas models. Figure 12a depicts the frequencies of the aeroelastic system as a function of flutter Mach number. The different lines correspond to different turbulence assumptions. In Fig. 12b, the damping coefficients are affected by the gas model. Changing the gas model from PG to IG affects the flutter boundary by about 2%. The difference between IG and RG is 1%.

The flutter boundaries calculated at the altitudes of 15 and 21 km are presented in Figs. 13a and 13b. In Fig. 13a, the effect of turbulence is considered. Laminar flow (Lam.) is compared to turbulent flows (Turb.). Note that the flutter boundaries are very close to each other and also close to that obtained with PT. The results labeled Modified Turb. correspond to a modified SA turbulence model. The CFD++ code is used with the SA turbulence model, similar to the turbulent

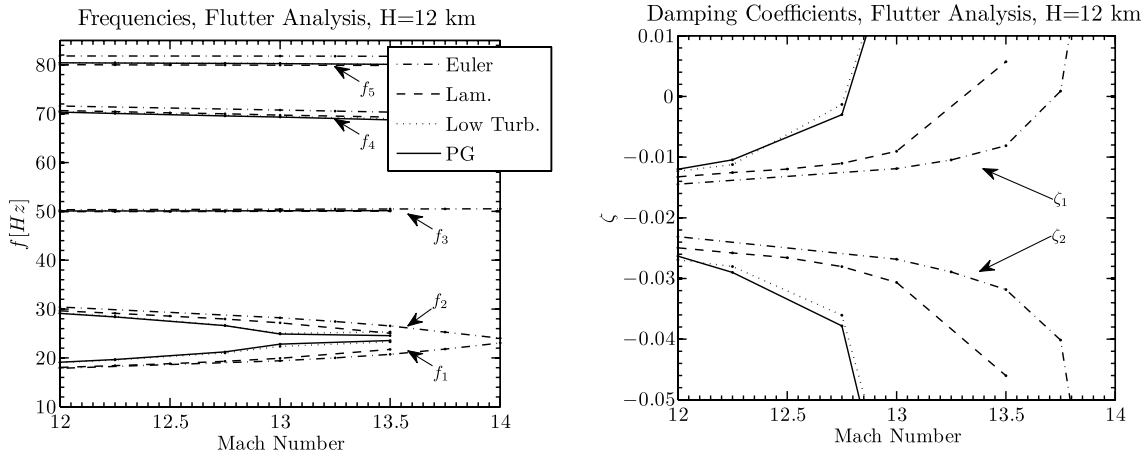

a) Frequencies **b) Damping Coefficients**

Fig. 11 Aeroelastic-stability boundary for different turbulent flows, $H = 12$ km.

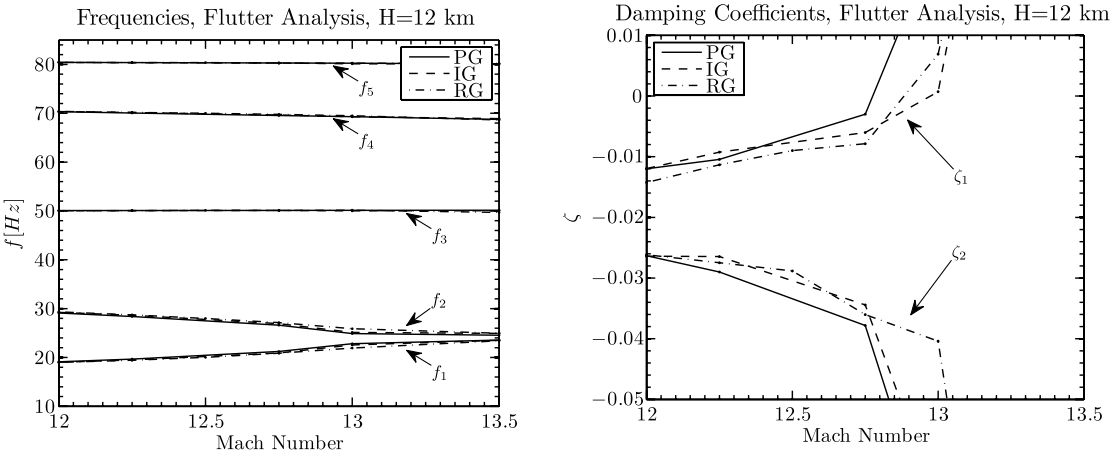

a) Frequencies **b) Damping coefficients**

Fig. 12 Aeroelastic-stability boundary for different gas models, $H = 12$ km.

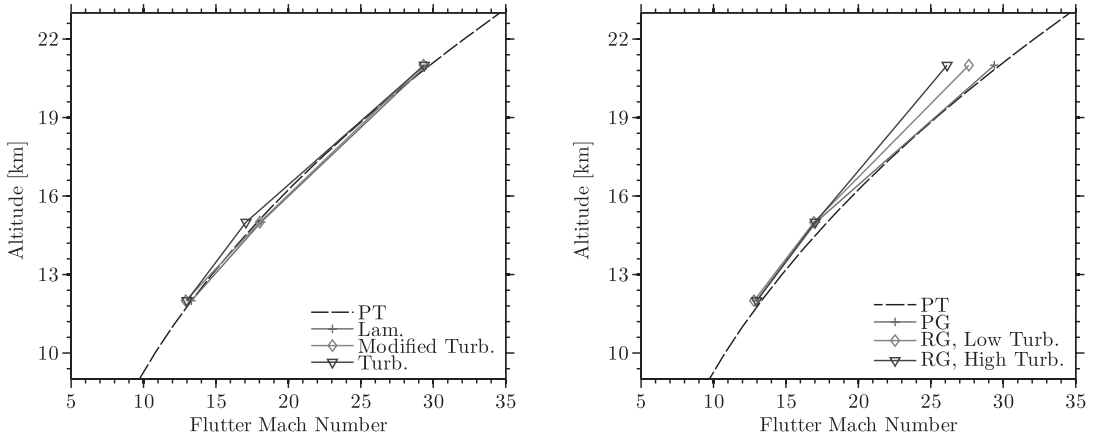

a) Effect of turbulence **b) Effect of gas model**

Fig. 13 Flutter boundaries for different gas models and turbulence models.

case; however, the coefficients of the SA model are modified to match the ones in the CFL3D code implementation. There is a small change in flutter boundary. It seems that the CFL3D code predicts a flow that is less turbulent than that with CFD++, which is the reason for the difference in the flutter-boundary calculations.

In Fig. 13b, the effect of gas modeling is investigated. The PG model is compared to RG. The flutter boundaries are very close to each other and close to that with PT. There is a small change in flutter boundary due to RG effects. The change is more significant at a higher Mach number, in which RG effects are more important. Similarly, as in the case of PG, adding turbulence decreases the flutter boundary.

Note that the altitudes 12–21 km, at which the aeroelastic studies are conducted, are not representative of hypersonic flight. More realistic altitudes of 20–30 km produce very high flutter Mach numbers, and therefore, the altitude is artificially reduced to reduce these to practical values. However, as pointed out in [35], incorporation of aerodynamic heating leads to a reduction of the flutter Mach number, and thus, aerothermoelastic studies can be conducted at more reasonable altitudes. Therefore, in the following section, aerodynamic heating is added.

C. Aerothermoelastic Results

The vehicle is in straight and level flight, at a constant altitude H_f and Mach number M_∞. The flight conditions are summarized in Table 6. To investigate the effect of turbulence on the aerothermoelastic behavior of the wing, both laminar and turbulent heat fluxes are considered. In addition, transition is artificially incorporated by arbitrarily choosing the location of transition point, x_t/c, on the wing, and combining the laminar heat flux with that corresponding to turbulent flow. For a given trajectory, the influence of the transition location, x_t/c, is investigated by arbitrarily varying its location from the leading edge to the trailing edge of the wing.

Flutter boundaries based on CFD are in good agreement with those based on Lin. PT. Therefore, to limit the computational cost, PT was used for computing the results in this section.

The framework presented in Sec. II is used to study the aeroelastic stability of the heated structure on a straight and level trajectory. The important dependencies considered are listed as follows:

1) H_f, M_∞, x_t: A trajectory is characterized by altitude, Mach number, and also flow regime (laminar, turbulent, or transition location x_t).

2) $f_i(t, H_f, M_\infty, x_t)$: The natural frequencies and mode shapes of the heated structure are a function of time along a given trajectory.

3) $M_{\text{fm}}(H, t, H_f, M_\infty, x_t)$: For each time instant along a trajectory, there is a corresponding heated structure with its flutter margin expressed in terms of Mach number M_{fm} as a function of altitude H.

The detailed results are presented for a vehicle in level flight at Mach 8 and altitude $H_f = 30$ km, and are representative of the behavior of the structure at a different Mach number.

Table 6 Flight conditions considered

Parameter	Value	Unit
H_f	30	km
M_∞	6–15	N/A
x_t/c	0–100	%

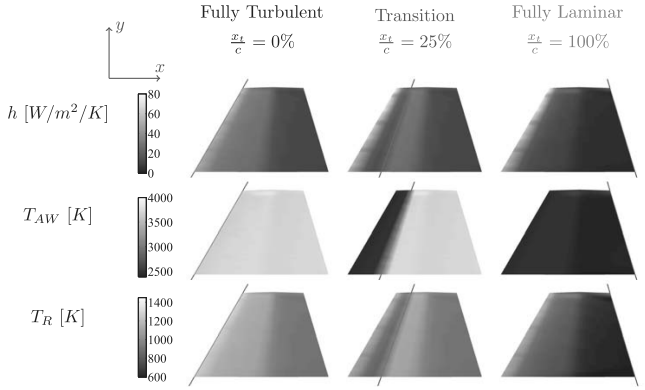

Fig. 14 Aerodynamic heating results for $M_\infty = 8$ and $H_f = 30$ km.

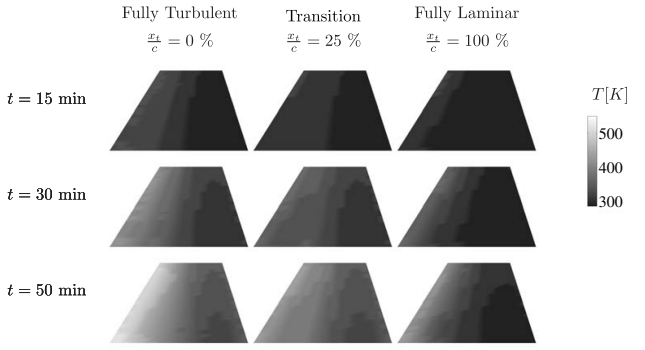

Fig. 15 Temperature distribution in the wing for $M_\infty = 8$ and $H = 30$ km.

The aerodynamic heat-flux results are presented in Fig. 14. The distribution of heat-flux coefficient, adiabatic-wall temperature, and equilibrium-radiation temperature is given by the color shading for three cases: fully turbulent flow, transition flow with $x_t/c = 25\%$, and fully laminar flow. The line crossing the wing from its root to its tip, at constant x_t/c, indicates the transition location. From the leading edge of the wing to transition, the flow is laminar. Downstream the transition point, the flow is turbulent.

High heat-flux coefficient at the leading edge of the wing is obtained for all cases. The enhanced heating in the front half of the wing produces higher radiation equilibrium temperature T_R on the surface of the wing. Note that the heat flux in laminar flow is an order of magnitude smaller than its value for fully turbulent flows. Thus, incorporating transition on the surface of the wing generates heat-flux gradients producing temperature gradients on the wing.

The thermal-analysis results are shown in Fig. 15. The different times, $t = 15$, 30, and 50 min along the trajectory, are considered. Temperature distributions on the wing are given for three heat fluxes corresponding to laminar, turbulent, and transition flow. After a flight time of 15 min, the temperatures in the load-carrying structure are close to the initial temperature of 288 K. As the wing heats up, the temperature rises. For laminar and turbulent flow, the temperature decreases smoothly from the leading edge to the trailing edge of the wing. The maximum temperature occurs in turbulent flow, and reaches 513 K after 50 min. As expected, the wing in laminar flow has the lowest temperature increase. For a wing experiencing transition on its surface, the temperature decreases up to the transition location where a small increase occurs. From the transition location to the trailing edge, the temperature decreases smoothly. The transition on the surface of the wing affects the magnitude of the temperature in the wing, as well as its distribution.

In Fig. 16, the results from a modal analysis for a vehicle in level flight, at $M = 8$ and an altitude of $H_f = 30$ km, are shown for three different times: $t = 15$, 30, and 50 min along the trajectory. At each time, the frequencies of the heated structure are provided as a function of the flow conditions: from fully turbulent for $x_t/c = 0$ to fully laminar for $x_t/c = 100\%$. The thin horizontal lines correspond to the natural frequencies of the cold structure, and are given for reference. Note that the natural frequencies decrease faster for the case of turbulent flow, $x_t = 0$, than for laminar flow, $x_t = c$. The lower frequencies for the case of turbulent flow are to be expected due to the higher heat flux. For flow with transition in the first half of the wing, the heated frequencies are much lower for $t = 30$ min and $t = 50$ min. However, the behavior of a wing with transition on its

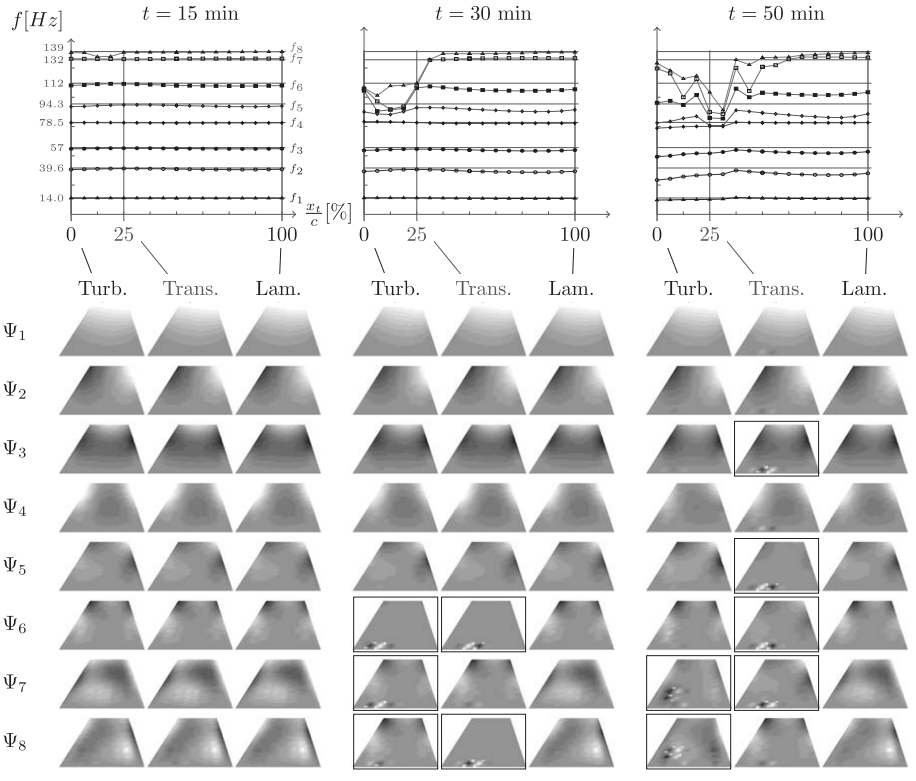

Fig. 16 Modal analysis of the heated structure for $M_\infty = 8$ and $H = 30$ km.

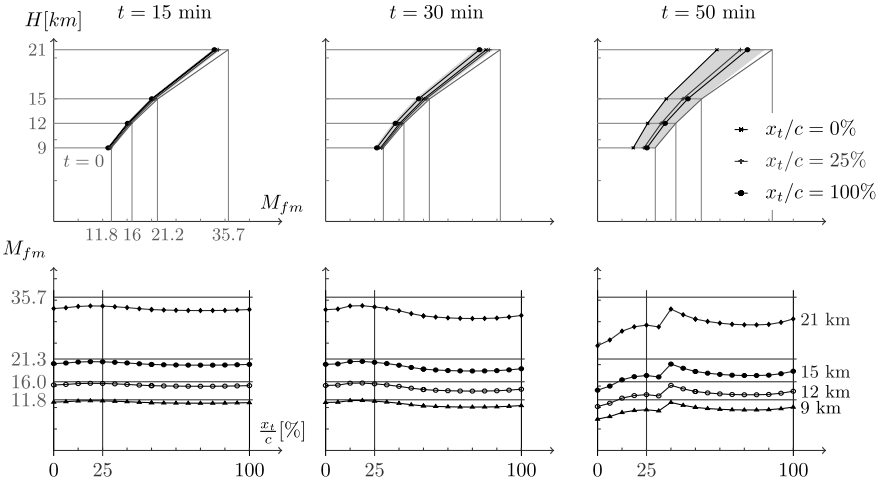

Fig. 17 Flutter margin of the heated structure for $M_\infty = 8$ and $H_f = 30$ km.

surface does not lie between that for either fully turbulent or fully laminar flow. Nonlinearities due to thermal stresses occur and significantly affect the structural integrity of the wing.

It is important to relate these frequencies to their corresponding mode shapes. For each instant in time, the first eight mode shapes are depicted for three flow conditions: turbulent (Turb.), transition located at $x_t/c = 25\%$ (Trans.), and laminar (Lam.). All the mode shapes are normalized, such that the magnitude of the maximum displacement is 1. The dark color corresponds to a value of -1, and white to a value of $+1$. At $t = 15$ min, the mode shapes corresponding to the three heating conditions are similar to that of the cold structure. However, at $t = 30$ min and $t = 50$ min, new mode shapes appear and are highlighted by an enclosing rectangle. These mode shapes are not present in the unheated structure or at the beginning of the trajectory. Due to the increased temperature and the resulting thermal stresses, the first eight modes are modified. The new modes display local buckling due to thermal stresses.

1. *Flutter Boundaries*

The exact flutter boundaries are determined by fixing a flight duration, t_f, and by finding the flight Mach number M_∞ at which the flutter margin M_{fm} is M_∞ after t_f. This approach required a sequential iteration on M_∞ until convergence to a flutter margin is achieved. Eventually, the Mach number defines the flutter boundary after t_f.

To illustrate this process, a flight condition characterized by $H_f = 20$ km, with $t_f = 30$ min, is considered. The initial flight Mach number $M_\infty = 10$ yields a flutter margin of $M_{\text{fm}} = 33.5$ after 30 min of level flight. The Mach number is updated to $M_\infty = 10 + 33.5/2 = 21.7$. At this flight condition, the wing buckles before it flutters, and the flutter boundary does not converge. Similarly, at $H_f = 30$ km, the initial $M_\infty = 10$ yields a flutter margin of $M_{\text{fm}} = 59.0$. The Mach number is updated to $M_\infty = 10 + 59.0/2 = 34.5$. At this flight condition, the wing buckles before it flutters, and the flutter boundary does not converge either. The implication of this behavior is that the iterative procedure for updating the flutter margin leads to local buckling, which is the main cause of failure.

2. *Flutter Margins*

The results presented in this section correspond to flutter margins of the heated wing. In [2], such a flutter margin is referred to as a virtual flutter boundary. In Fig. 17, the flutter margins for a vehicle in level flight at $M = 8$ and an altitude of 30 km are provided at three different times: $t = 15$, 30, and 50 min. At each time, the flutter margins are given in terms of the flutter-margin Mach number M_{fm} as a function of altitude H, and for three flow conditions: turbulent ($x_t/c = 0$), transition located at $x_t/c = 25\%$ (Trans.), and laminar ($x_t/c = 1$). The shaded region corresponds to the range of flutter margins as the transition location is moved from the leading edge of the wing to its trailing edge. The thin line corresponds to the flutter margin of the cold structure, and is provided for reference. The same flutter margins are provided in the lower portion of the figure as a function of the transition location x_t for four different altitudes of $H = 9$, 12, 15, and 21 km. Note that the flutter margin for the structure under turbulent heating always corresponds to the lowest one. However, the margin for laminar case is not necessarily the highest. Depending on the transition location, the flutter margin of the heated wing can vary significantly. This highlights the importance of the thermal stresses that influence the aeroelastic stability of the heated structure.

In Fig. 18, the variations of aeroelastic-stability margin for an altitude of $H = 12$ km are given as a function of time for the three different flow conditions highlighted previously. The behavior of the flutter margins corresponding to 9, 15, and 21 km is similar. The darker shaded area corresponds to cases without thermal stresses. When only material degradation is considered, the flutter margins are decreased by less than 5% after an hour of flight. The wing under turbulent flow has the lowest margin, and that under laminar flow has

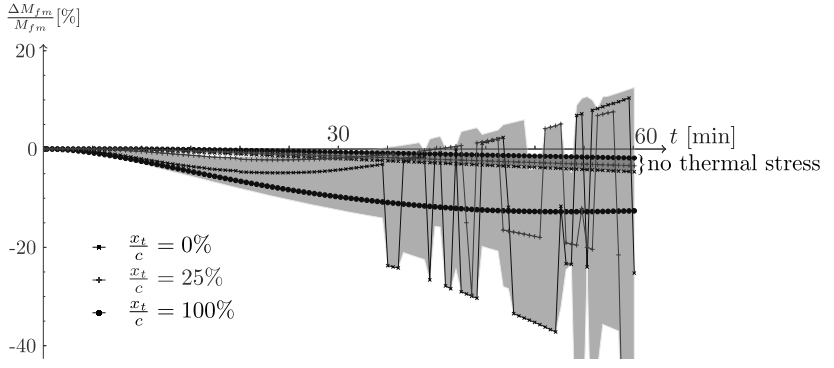

Fig. 18 Variation of aeroelastic-stability margin of the heated structure for $M_\infty = 8$ and $H_f = 30$ km.

Table 7 Aerothermoelastic behavior

Trajectory		With thermal stresses: max(ΔM_{fm}), %	With thermal stresses: t_f, min	No thermal stresses: max(ΔM_{fm}), %	No thermal stresses: t_f, min
$M_\infty = 8$	Laminar	−12.7	>60	−1.9	—
	$x_t/c = 25\%$	−2.2	35	−3.4	—
	Turbulent	−4.8	34	−4.6	—
$M_\infty = 10$	Laminar	−13.2	54	−3.4	—
	$x_t/c = 25\%$	−0.9	22	−6.1	—
	Turbulent	−3.3	18	−8.6	—

the highest margin. The wing experiencing transition at its surface has an intermediate flutter margin. When thermal stresses are accounted for, the behavior of the heated wing is not as intuitive anymore as depicted with the lighter shaded area. Note that discontinuities start to occur after 35 min of flight time for the wing under turbulent flow, and after 34 min under transition flow. These discontinuities are due to the high levels of thermal stresses and thermal degradation that develop in the structure. Before these flight times, the flutter margins are from the lowest to the highest for the wing under laminar, turbulent, and transition flows. This order is counterintuitive and is caused by increasing thermal stresses. Turbulent flows generate high heat flux and high temperature in the wing; however, transition at the surface of the wing causes higher temperature gradients.

The aerothermoelastic results are summarized in Table 7. The time t_f denotes the flight time. It corresponds to the instance of time when the first discontinuity in the aeroelastic margins occurs. The maximum drop in aeroelastic-stability margin, $\Delta M_{\text{fm}} = M_{\text{fm}}(t) - M_{\text{fc}}$, before t_f is also provided. The variation in stability margin is normalized with respect to the flutter Mach number of the cold structure M_{fc}. The wing under turbulent flows is the first to buckle, reflected by its significant loss in aeroelastic-stability margin. However, in the early part of the flight, the wing under laminar flows has the highest decrease in flutter margin.

Further details are given in Fig. 19. The time to buckling is given as a function of transition location and M_∞ for $H_f = 30$ km. At Mach 7 and 8, the wing buckles only for transition located before $x_t = 25$ and 40%, respectively. At Mach 10, the buckling time is the lowest for transition located in the first half of the wing, and does not vary much, close to 55 min for transition located in the second half of the wing. When $x_t = 75\%$, the wing does not buckle in the first hour of flight; this situation is indicated by the gap in the curve.

These results highlight the importance of nonlinearities due to transitional flow and thermal stresses in the aerothermoelastic behavior of the structure [53]. It is not sufficient to consider only turbulent or laminar flow conditions because transition on the surface of the wing can significantly alter its structural behavior.

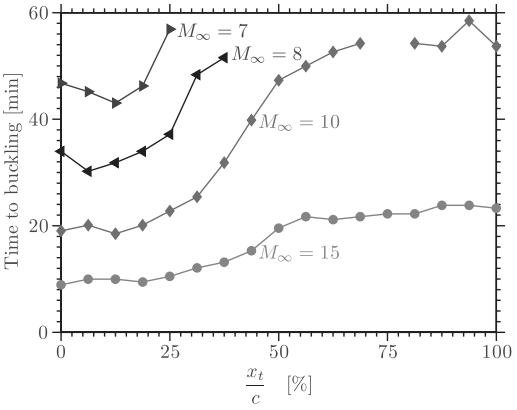

Fig. 19 Time to buckling as a function of transition location.

D. Uncertainty-Propagation Results

In this section, the UQ is used to examine the hypothesis that fully turbulent flow is a conservative assumption. Therefore, the transition location is considered as an uncertain variable. The output of interest is the flutter margin as a function of time.

The probability of failure, defined by Eq. (42), is the probability that the flutter Mach number is less than that predicted under the hypothetical conservative assumption of fully turbulent flow:

$$p_f(t) = p[M_{\text{fm}}(t, x_t) < M_{\text{fm}}(t, x_t = 0)] = \int_{M_{\text{fm}}(t,x_t)<M_{\text{fm}}(t,0)} p_{x_t}(x_t)\,\mathrm{d}x_t \tag{42}$$

If fully turbulent flows correspond to the worst-case scenario, the probability of failure is 0. The p_f represents the degree of error associated with the assumption that turbulent flow is a lower bound for the behavior of the heated wing.

The transition location is the uncertain variable; however, its probability distribution is unknown. Intuitively, transition is more likely to occur closer to the leading edge. Therefore, the PDF of the transition location is assumed to be Beta(1, 3) for the illustrative example presented here. Further research on transition modeling is needed to fully assess the possible location of transition location and its likelihood. However, this work is beyond the scope of this paper.

For $t > t_f$, the relation between flutter margin and transition location, $M_{\text{fm}} = f(x_t)$, is highly nonlinear, reflecting buckling. Therefore, polynomial response surfaces such as SC failed to converge. In addition, kriging and spline interpolations were considered,

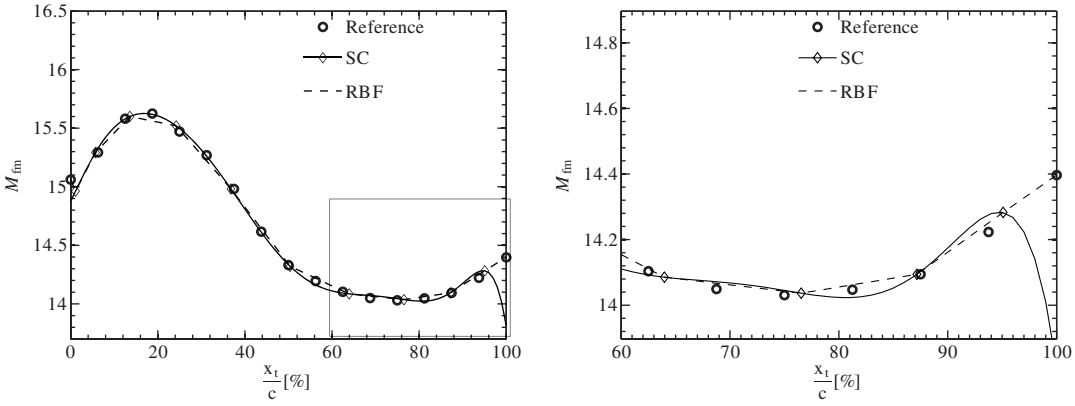

a) Response surface **b) Closer view at $x_t = c$**

Fig. 20 Flutter Mach-number response surfaces for Beta(1,3) PDF.

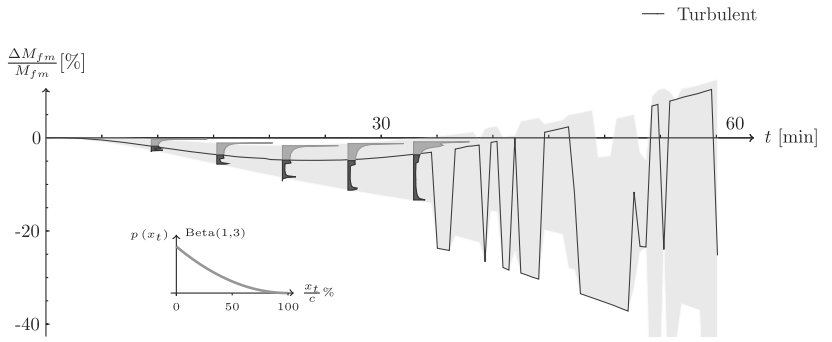

Fig. 21 Uncertainty-propagation results for the flutter margin, $H = 12$ km.

but failed to converge as well [54]. Therefore, UQ results are generated for $t < t_f$.

The prediction of the response surface is compared to the exact value at 17 uniformly distributed points to quantify the error of the response surface. Results from the SC and RBF methods are illustrated in Fig. 20 for $M_\infty = 8$, $H_f = 30$ km, $H = 12$ km, and $t = 27$ min. The SC indicates oscillations close to the trailing edge at $x_t = c$. The response surfaces are given in Fig. 20a for the case of Beta$(1, 3)$. Figure 20b corresponds to a closer view of the region delimited by a box in Fig. 20a. The RBF interpolation gives a better approximation than SC. Note that the SC approach predicts lower values of flutter Mach numbers at $x_t = c$, and therefore, does not predict accurately the range of M_{fm}. The bad performance of this polynomial-based approach is due to the strongly nonlinear relation between x_t and M_{fm}, which cannot be approximated by global polynomials. Furthermore, the polynomial response surfaces are based on a limited number of points, and require extrapolation at the edges of the design space, which adversely affects accuracy. Therefore, the RBF-based response surface using volume spline is a useful and reliable alternative, and is used for the results presented in this section. For the cases presented next, the mean error of the response surface was less than 0.3% of the deterministic value.

The results of the uncertainty propagation are given in Fig. 21, for $M_\infty = 8$ and $H_f = 30$ km, and a flutter margin at $H = 12$ km. The assumed probability of the transition location is depicted in the figure. The PDF of the variation of flutter margin is given for six time

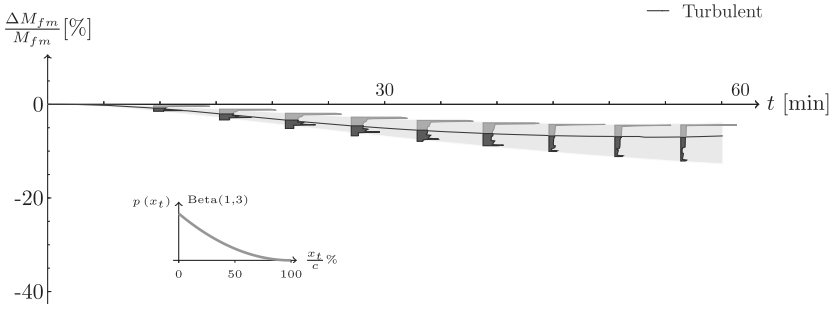

a) $M_\infty = 6$

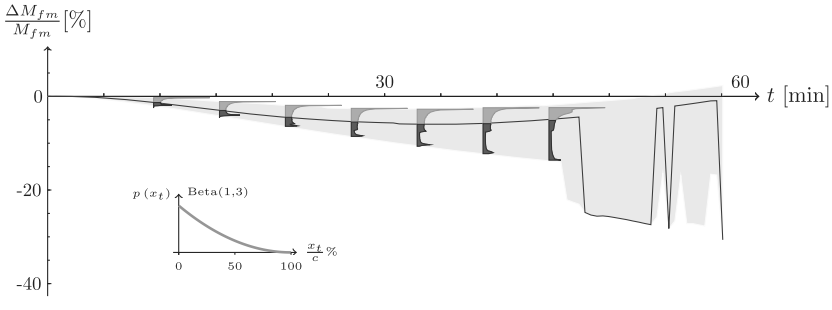

b) $M_\infty = 7$

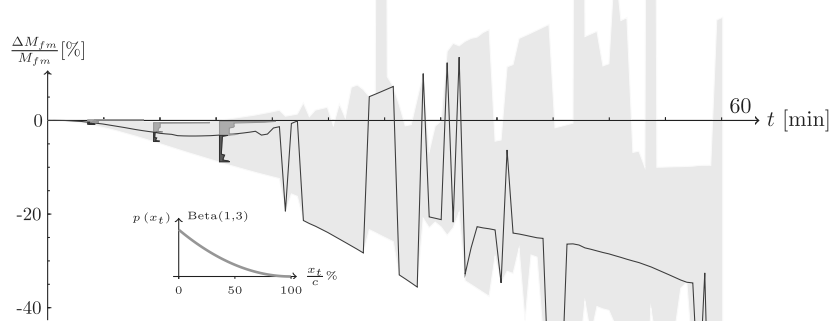

c) $M_\infty = 10$

Fig. 22 Uncertainty-propagation results for the flutter margin, $H = 12$ km.

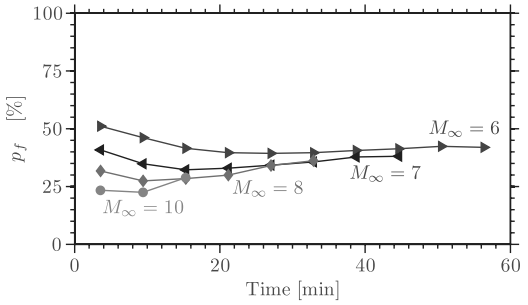

Fig. 23 Probability of failure as a function of time for $p(x_t)=p_{(1,3)}(x_t)$.

instants, and these are superimposed on the deterministic results presented in the previous section. The darker shading of the PDF corresponds to the cases when the flutter margin is less than that predicted for fully turbulent, quantifying the probability of failure p_f.

Additional results for $M_\infty = 6$, 7, and 10 are presented in Figs. 22a–22c, respectively. The transition location is assumed to be distributed according to the Beta(1, 3) distribution. The PDF of the variation of flutter Mach number is shown for the time instants before buckling occurs.

The probability of failure p_f indicates the probability that the stability margin may be less than that predicted for turbulent flows, given in Fig. 23. Depending on the Mach number, the chances that the stability margin is less than the one predicted using fully turbulent flows vary between 25 and 50%. These results illustrate that the turbulent case is not the worst case possible.

V. Conclusions

A framework for hypersonic aerothermoelastic calculation using PT and CFD is presented. The results demonstrate that deterministic quantification of aeroelastic- and aerothermoelastic-stability boundaries may be inadequate for hypersonic-vehicle analysis. The principal conclusions are summarized as follows:

1) A new linearization of PT is presented. It shows that, for aeroelastic-stability studies, the generalized loads are a linear function of the generalized degrees of freedom and their time derivative.

2) Based on the results obtained with PT, a robust SI method for determining the flutter speed has been developed.

3) The RBF approach is a robust and efficient mesh-deformation scheme. However, the exact geometrical shape is not preserved throughout the deformation unless a sufficient number of driving points are used.

4) This is the first study to explore the effects of RG models on aeroelastic stability in a systematic manner. RG effects modify the aeroelastic-stability boundary by 2–6%, at the flight conditions considered.

5) Turbulence modeling introduces a degree of uncertainty in the calculation of aeroelastic-stability margins. An increase in the boundary-layer thickness increases the aerodynamic loading. Thus, viscosity reduces the flutter margin.

6) The behavior of the wing in high-speed flight is strongly dependent on the thermal stresses. Thermal buckling causes a significant loss in aeroelastic-stability margins. Turbulent flow enhances aerodynamic heating, producing short flight times to failure when compared to laminar flow.

7) Transition is a key parameter for the aerothermoelastic behavior of the wing. It significantly affects the thermal problem and the aerothermoelastic behavior of the wing. Transition at the surface of the wing creates temperature gradients in the load-carrying structure, which modify thermal stresses and structural properties. Investigating the limiting cases of turbulent or laminar flow is not sufficient when transition is likely to occur on the structure.

Acknowledgments

This research was funded under NASA grant NNX08AB32A, with Donald Soloway and Jorge Bardina as technical monitors. Partial support was provided by the Michigan/U.S. Air Force Research Laboratory Collaborative Center in Aeronautical Sciences, via grant Air Force grant FA8650-06-2-3625. The authors would like to acknowledge the help of Jack J. McNamara from The Ohio State University, and Beerinder Singh from Metacomp Technologies.

References

[1] McNamara, J. J., and Friedmann, P. P., "Aeroelastic and Aerothermoelastic Analysis in Hypersonic Flow: Past, Present, and Future," *AIAA Journal*, Vol. 49, No. 6, 2011, pp. 1089–1122. doi:10.2514/1.J050882

[2] McNamara, J. J., "Aeroelastic and Aerothermoelastic Behavior of Two and Three Dimensional Lifting Surfaces in Hypersonic Flow," Ph.D. Thesis, Univ. of Michigan, Ann Arbor, MI, 2005.

[3] Fidan, B., Mirmirani, M., and Ioannou, P. A., "Flight Dynamics and Control of Air-Breathing Hypersonic Vehicles: Review and New Directions," *12th AIAA International Space Planes and Hypersonic Systems and Technologies*, AIAA Paper 2003-7081, Dec. 2003.

[4] Hallion, R. P., "The History of Hypersonics: or, 'Back to the Future—Again and Again'," *43rd AIAA Aerospace Sciences Meeting and Exhibit*, AIAA Paper 2005-0329, Jan. 2005.

[5] Rodriguez, A. A., Dickeson, J. J., Cifdaloz, O., Kelkar, A., Vogel, J. M., and Soloway, D., "Modeling and Control of Scramjet-Powered Hypersonic Vehicles: Challenges, Trends, and Tradeoffs," *AIAA Guidance, Navigation and Control Conference and Exhibit*, AIAA Paper 2008-6793, Aug. 2008.

[6] Dolvin, D. J., "Hypersonic International Flight Research and Experimentation (HIFiRE), Fundamental Sciences and Technology Development Strategy," *15th AIAA International Space Planes and Hypersonic Systems and Technologies Conference*, AIAA Paper 2008-2581, April–May 2008.

[7] Bertin, J. J., *Hypersonic Aerothermodynamics*, AIAA Education Series, AIAA, Washington, D.C., 1994, pp. 335–439.

[8] Anderson, J. D., *Modern Compressible Flow with Historical Perspective*, 3rd ed., McGraw–Hill, New York, 2004, pp. 585–644.

[9] Hayes, W. D., and Probstein, R. F., "Inviscid Flows," *Hypersonic Flow Theory*, Vol. 1, Academic Press, New York, 1966, Chaps. 1–2.

[10] Dugundji, J., and Calligeros, J. M., "Similarity Laws for Aerothermoelastic Testing," *Journal of the Aerospace Sciences*, Vol. 29, No. 8, Aug. 1962, pp. 935–950.

[11] Fry, R., "A Century of Ramjet Propulsion Technology Evolution," *Journal of Propulsion and Power*, Vol. 20, No. 1, 2004, pp. 27–58. doi:10.2514/1.9178

[12] Jenkins, D. R., "Hypersonics Before the Shuttle: A Concise History of the X-15 Research Airplane," NASA History Series Publications, Vol. 4518, Monographs in Aerospace History, Issue 18," NASA, Washington, D.C., 2000, pp. 118–122.

[13] Merlin, P., "Design and Development of the Blackbird: Challenges and Lessons Learned," *47th AIAA Aerospace Sciences Meeting Including the New Horizons Forum and Aerospace Exposition*, AIAA Paper 2009-1522, Jan. 2009.

[14] Heppenheimer, T. A., "Facing the Heat Barrier: A History of Hypersonics," NASA SP-2007-4232, NASA History Series, 2007.

[15] Augenstein, B. W., et al., *The National Aerospace Plane (NASP): Development Issues for the Follow-On Vehicle*, RAND Corp., Santa Monica, CA, 1993, pp. 14–29.

[16] Lighthill, M. J., "Oscillating Airfoils at High Mach Number," *Journal of the Aeronautical Sciences*, Vol. 20, No. 6, 1953, pp. 402–406. doi:10.2514/8.2657

[17] Ashley, H., and Zartarian, G., "Piston Theory—A New Aerodynamic Tool for the Aeroelastician," *Journal of the Aeronautical Sciences*, Vol. 23, No. 12, 1956, pp. 1109–1118.

[18] *CFD++ User Manual, Ver. 10.1*, Metacomp Technologies, Agoura Hills, CA, 2010.

[19] MacNeal, R., "NASTRAN Theoretical Manual," NASA Scientific and Technical Information Office, 1981.

[20] Roy, C. J., and Blottner, F. G., "Review and Assessment of Turbulence Models for Hypersonic Flows," *Progress in Aerospace Sciences*, Vol. 42, Nos. 7–8, 2006, pp. 469–530. doi:10.1016/j.paerosci.2006.12.002

[21] Lamorte, N., and Friedmann, P. P., "Hypersonic Aeroelastic Stability Boundary Computations Using Radial Basis Functions for Mesh Deformation," *18th AIAA/3AF International Space Planes and Hypersonic Systems and Technologies Conference*, AIAA Paper 2012-5943, Sept. 2012.

[22] Schütte, G., and Staudacher, S., "Probabilistic Aspects of Scramjet Design," *Journal of Propulsion and Power*, Vol. 25, No. 2, 2009,

pp. 281–288.
doi:10.2514/1.38195
[23] Eldred, M. S., and Burkardt, J., "Comparison of Non-Intrusive Polynomial Chaos and Stochastic Collocation Methods for Uncertainty Quantification," *47th AIAA Aerospace Sciences Meeting Including the New Horizons Forum and Aerospace Exposition*, AIAA Paper 2009-0976, Jan. 2009.
[24] Lamorte, N., Friedmann, P. P., Glaz, B., Culler, A. J., Crowell, A. R., and McNamara, J. J., "Uncertainty Propagation in Hypersonic Aerothermoelastic Analysis," *Journal of Aircraft*, Vol. 51, No. 1, 2014, pp. 192–203.
doi:10.2514/1.C032233
[25] Lamorte, N., Friedmann, P., Dalle, D., Torrez, S., and Driscoll, J., "Uncertainty Propagation in Integrated Airframe Propulsion System Analysis for Hypersonic Vehicles," *17th AIAA International Space Planes and Hypersonic Systems and Technologies Conference*, AIAA Paper 2011-2394, April 2011.
[26] Boley, B. A., and Weiner, J. H., *Theory of Thermal Stresses*, Dover Civil and Mechanical Engineering Series, Dover, New York, 2012, Chap. 2.
[27] McNamara, J. J., and Friedmann, P. P., "Flutter Boundary Identification for Time-Domain Computational Aeroelasticity," *AIAA Journal*, Vol. 45, No. 7, 2007, pp. 1546–1555.
doi:10.2514/1.26706
[28] Bartels, R., Rumsey, C., and Biedron, R., "CFL3D Version 6.4, General Usage and Aeroelastic Analysis," NASA TM-2006-214301, 2006.
[29] Higham, N. J., "The Scaling and Squaring Method for the Matrix Exponential," *SIAM Journal on Matrix Analysis and Applications*, Vol. 26, No. 4, 2005, pp. 1179–1193.
doi:10.1137/04061101X
[30] Buhmann, M. D., *Radial Basis Functions: Theory and Implementations*, Cambridge Univ. Press, Cambridge, England, U.K., 2003, pp. 99–162.
[31] Park, C., *Nonequilibrium Hypersonic Aerothermodynamics*, Wiley-Interscience, New York, 1990, pp. 255–327.
[32] Hassig, H. J., "An Approximate True Damping Solution of the Flutter Equation by Determinant Iteration," *Journal of Aircraft*, Vol. 8, No. 11, 1971, pp. 885–889.
doi:10.2514/3.44311
[33] Rodden, W. P., *Theoretical and Computational Aeroelasticity*, Crest Publishing, Burbank, CA, 2011, Chap. 7.
[34] Crassidis, J. L., and Junkins, J. L., *Optimal Estimation of Dynamic Systems*, Applied Mathematics and Nonlinear Science Series, Chapman & Hall/CRC Press, Boca Raton, FL, 2004, pp. 1–52.
[35] McNamara, J. J., Friedmann, P. P., Powell, K. G., Thuruthimattam, B. J., and Barrels, R. E., "Aeroelastic and Aerothermoelastic Behavior in Hypersonic Flow," *AIAA Journal*, Vol. 46, No. 10, 2008, pp. 2591–2610.
doi:10.2514/1.36711
[36] Haldar, A., and Mahadevan, S., *Probability, Reliability and Statistical Methods in Engineering Design*, Wiley, New York, 2000, pp. 35–105.
[37] Ghanem, R. G., and Spanos, P. D., *Stochastic Finite Elements, a Spectral Approach*, Rev. ed., Dover, New York, 1991, pp. 1–20.
[38] Mathelin, L., Hussaini, M. Y., and Zang, T. A., "Stochastic Approaches to Uncertainty Quantification in CFD Simulations," *Numerical Algorithms*, Vol. 38, No. 1, 2005, pp. 209–236.
doi:10.1007/s11075-004-2866-z
[39] Walters, R. W., "Towards Stochastic Fluid Mechanics via Polynomial Chaos," *41st Aerospace Sciences Meeting and Exhibit*, AIAA Paper 2003-0413, Jan. 2003.
[40] Witteveen, J., Loeven, A., and Bijl, H., "An Adaptive Stochastic Finite Elements Approach Based on Newton–Cotes Quadrature in Simplex Elements," *Computers & Fluids*, Vol. 38, No. 6, 2009, pp. 1270–1288.
[41] Eldred, M. S., Webster, C. G., and Constantine, P. G., "Design Under Uncertainty Employing Stochastic Expansion Methods," *12th AIAA/ISSMO Multidisciplinary Analysis and Optimization Conference*, AIAA Paper 2008-6001, Sept. 2008.
[42] Murugan, S., Harursampath, D., and Ganguli, R., "Material Uncertainty Propagation in Helicopter Nonlinear Aeroelastic Response and Vibration Analysis," *AIAA Journal*, Vol. 46, No. 9, 2008, pp. 2332–2344.
doi:10.2514/1.35941
[43] Pettit, C., "Uncertainty Quantification in Aeroelasticity: Recent Results and Research Challenges," *Journal of Aircraft*, Vol. 41, No. 5, Sept.–Oct. 2008, pp. 1217–1229.
[44] Hosder, S., Walters, R. W., and Balch, M., "Efficient Uncertainty Quantification Applied to the Aeroelastic Analysis of a Transonic Wing," *46th AIAA Aerospace Sciences Meeting and Exhibit*, AIAA Paper 2008-0729, Jan. 2008.
[45] Styuart, A. V., Livne, E., Demasi, L., and Mor, M., "Flutter Failure Risk Assessment for Damage-Tolerant Composite Aircraft Structures," *AIAA Journal*, Vol. 49, No. 3, 2011, pp. 655–669.
doi:10.2514/1.J050862
[46] Lindsley, N. J., Beran, P. S., and Pettit, C. L., "Integration of Model Reduction and Probabilistic Techniques with Deterministic Multi-Physics Models," *44th AIAA Aerospace Sciences Meeting and Exhibit*, AIAA Paper 2006-0192, Jan. 2006.
[47] Lindsley, N. J., Beran, P. S., and Pettit, C. L., "Effects of Uncertainty on Nonlinear Plate Response in Supersonic Flow," *9th AIAA/ISSMO Symposium on Multidisciplinary Analysis and Optimization*, AIAA Paper 2002-5600, Sept. 2002.
[48] Beran, P. S., and Pettit, C. L., "A Direct Method for Quantifying Limit-Cycle Oscillation Response Characteristics in the Presence of Uncertainties," *45th AIAA/ASME/ASCE/AHS/ASC Structures, Structural Dynamics, and Materials Conference*, AIAA Paper 2004-1695, April 2004.
[49] Kurdi, M., Lindsley, N., and Beran, P., "Uncertainty Quantification of the Goland Wing's Flutter Boundary," *AIAA Atmospheric Flight Mechanics Conference and Exhibit*, AIAA Paper 2007-6309, Aug. 2007.
[50] Choi, S.-K., Grandhi, R. V., Canfield, R. A., and Pettit, C. L., "Polynomial Chaos Expansion with Latin Hypercube Sampling for Estimating Response Variability," *AIAA Journal*, Vol. 42, No. 6, 2004, pp. 1191–1198.
doi:10.2514/1.2220
[51] Golub, G. H., and Welsch, J. H., "Calculation of Gauss Quadrature Rules," *Mathematics of Computation*, Vol. 23, No. 106, April 1969, pp. 221–230.
doi:10.1090/S0025-5718-69-99647-1
[52] Spalart, P. R., and Allmaras, S. R., "A One-Equation Turbulence Model for Aerodynamic Flows," *30th Aerospace Sciences Meeting and Exhibit*, AIAA Paper 1992-0439, Jan. 1992.
[53] Lamorte, N., and Friedmann, P. P., "Aerothermoelastic and Aeroelastic Studies of Hypersonic Vehicles Using CFD," *54th AIAA/ASME/ASCE/AHS/ASC Structures, Structural Dynamics, and Materials Conference*, AIAA Paper 2013-1591, April 2013.
[54] Lamorte, N., "Uncertainty Propagation in Hypersonic Vehicle Aerothermoelastic Analysis," Ph.D. Thesis, Univ. of Michigan, Ann Arbor, MI, 2013.

W. Silva
Associate Editor